Ultrasonics - Sonochemistry 49 (2018) 175–189

Contents lists available at ScienceDirect

Ultrasonics - Sonochemistry

journal homepage: www.elsevier.com/locate/ultson

Facile synthesis, growth process, characterisation of a nanourchin-structured α-MnO_2 and their application on ultrasonic-assisted adsorptive removal of cationic dyes: A half-life and half-capacity concentration approach

Ria Abraham, Sarah Mathew, Susanna Kurian, M.P. Saravanakumar, Anu Mary Ealias*, Giphin George*

School of Civil and Chemical Engineering, Vellore Institute of Technology, Vellore Campus, Vellore 632014, India

ARTICLE INFO

Keywords:
Nanourchins
α-MnO_2
Ultrasonication
Dye adsorption
Isotherm-kinetics
Reusability

ABSTRACT

Textile dyes pose a serious threat in terms of water pollution due to its complex aromatic structures and poor degradability. In order to reduce the toxic effects of Crystal Violet (CV) and Methylene Blue (MB), an ultrasonic-assisted dye adsorption using urchin like α-MnO_2 nanostructures was studied. The adsorbent was synthesised by hydrothermal method at low-temperature. The crystallinity and morphology were determined to investigate the growth mechanism of α-MnO_2 nanourchins which consists of two main stages. The initial stage includes the formation of α-MnO_2 microspheres followed by the epitaxial growth of nanoneedles on to the surface of them. The α-MnO_2 was characterised by BET, XRD, FT-IR, XPS, SEM, TEM and TGA. At 5.6, the point of zero charge of α-MnO_2 nanostructures was determined. The total pore volume and average pore radius were confirmed to be 4.751×10^{-2} cc/g and 10.99 Å respectively from the BET analysis. Batch adsorption experiments were performed to investigate the effect of pH, adsorbent dosage, sonication time, initial dye concentration, temperature, ultrasonic frequency and power. The adsorption mechanism was studied using several isotherm and kinetic models. The adsorption data of CV and MB at equilibrium was observed to adopt the Langmuir isotherm model and pseudo-second order kinetic model. The maximum adsorption capacities for CV and MB were found to be 5882.3 and 5000 mg/g respectively. The thermodynamic study predicted that the process was exothermic for CV and endothermic for MB. The effects of competitive ions, ionic strength and humic acid on the uptake of both the dyes were also investigated. And finally, the reusability of recovered α-MnO_2 after dye adsorption was studied up to five cycles for its potential industrial applications.

1. Introduction

Rapid industrialisation and urbanisation have led to an increase in the amount of wastewater generated, leading to detrimental environmental impacts. Toxic organic dyes are present in the wastewater produced from the industrial units and are not susceptible to direct biological treatment [1,2]. Large quantities of dyes are produced annually from several industrial units such as textile, paper, food, cosmetic, leather and pharmaceuticals. 10–20% from 7,00,000 tonnes of dyes which are annually produced is being released into wastewater through the dyeing process from 1,00,000 commercially available dyes [3,4]. Organic dyes with complex aromatic structures possess a severe threat to the environment as they are chemically stable, strongly resistant to heat and light and are also non-biodegradable in water [1,5]. These dyes when present in the water bodies reduce light penetration through it and hence the photosynthetic process in aquatic plants are disturbed [5,6]. Degradation of dyes may generate toxic, carcinogenic and mutagenic compounds which cause severe risk to human beings and other living species [7]. So it's a necessity to treat this hazardous water using an adequate method so that maximum removal efficiency is obtained.

Among different conventional methods such as flocculation, coagulation, precipitation, ozonation, chemical oxidation and biological method membrane filtration [8,9], adsorption is the efficient and economically viable option for removing colour from industrial effluents [10]. Adsorption is the most broadly used method for treating large

* Corresponding authors.
E-mail addresses: anumaryealias@gmail.com (A. Mary Ealias), giphingeorge@gmail.com (G. George).

https://doi.org/10.1016/j.ultsonch.2018.07.045
Received 15 June 2018; Received in revised form 15 July 2018; Accepted 31 July 2018
Available online 03 August 2018
1350-4177/

quantities of water because of its simplicity, highly efficient removal capacity, fast recovery and adsorbent reusability [11]. The surface area of the nanomaterial, intraparticle interaction affinity and its strength are the major factors that determine the adsorption of the material [12,13]. Even though adsorption of industrial dyes is very complicated, economic feasibility promotes its wide acceptance around the world. The adsorbent used should be easily operatable, affordable and non-poisonous.

For the treatment of the industrial water, a sonocatalytic method is used which is a promising nominee to assist the physical, chemical and biological methods as it has a major benefit of high penetration ability in any fluid form [1]. Ultrasonic irradiation is mainly used to proliferate the chemical reaction with acoustic cavitation phenomenon. The generation, growth, as well as exhaustion of the micrometrical bubbles moulded by the dissemination of the pressure wave through a fluid, is a vital tool in which is used to intensify the mass transfer process. Thus an infringement bond was generated between the adsorbent and the adsorbate. A microscopic turbulence is created by the shock waves within the interfacial layer surrounding the dense particle [7]. The transformation of sound energy into kinetic energy is due to the motion of the liquid produced by the acoustic streaming of the sound waves. This process will increase the mass transfer near the dense surface [14]. The ultrasonic waves enhance the adsorptive removal of organic and inorganic pollutants. This hybrid technique has shown a significant synergetic effect on those pollutant removals. This system has already proven as an economically viable, effective and alternative technique for the wastewater treatment [15,16]. Recently, the application of the ultrasonication process in various industries [17] is being experimented with different population equivalent ranging from 50000 to 750000. A German-based company, Hielscher, supplies such a hybrid system to various domestic and industrial wastewater treatment plants [18]. Specifically, those sonication instruments have power up to 48 kW. Barber, has submitted a positive report on the application of ultrasound system from the results of industrial end users running in various countries like Germany, Austria, Italy etc. [19].

Manganese dioxide (MnO_2) is recognised as a favourable material because of its high stability, abundant availability, low cost and environmental compatibility [20]. The composites of nano manganese dioxide might act as degradant [21] and adsorbent [22,23] for various types of dyes and organic pollutants due to its octahedral crystal structure (MnO_6) with high redox potential and large surface area [24]. In this study Crystal Violet (CV) and Methylene Blue (MB) dyes has been selected, as it is economical and extensively used in the paper, pulp and textile industries [25]. CV is stated as a recalcitrant dye molecule that perseveres in the environment for a long time and causes hazardous effects on terrestrial as well as aquatic life [26,27]. Previous studies have shown that CV acts as a carcinogenic, mutagenic, clastogenic and encourages tumour growth in some fish species [26,28,29]. Therefore, the dye is considered as a biohazard substance. CV is also observed to cause enduring injury to conjunctiva and cornea, hurting light sensitisation, moderate eye irritation, meanwhile, the product comprises a cationic dye that is extremely toxic to living cells. However, in extreme cases, it may lead to kidney and respiratory failures also [30,31]. MB is a phenothiazine cationic dye [32] that has numerous negative effects on animals and human, such as nausea, increased heart rate and vomiting [33,34], and is inhibited to biodegradation due to its complex aromatic structure [35]. The adsorption using α- MnO_2 is not only selective to cationic dyes but also for anionic dyes. The previous study suggests that α- MnO_2 can be used for the effective removal of Congo red dye. Zhang et al. obtained a high monolayer adsorption capacity of 625 mg/g through the electrostatic attraction [36].

Various studies were conducted using ultrasonic-assisted adsorption for the removal of MB and CV dyes using different adsorbents. Reza et al. studied for the removal of MB using Cu: ZnS-NPs-AC [37] as the adsorbent and obtained the maximum adsorption capacity as 185.2 mg/g. Porhemmat et al. and Dashamiri et al. conducted experiments on MB dye adsorption using Co/Cu/S-TiO_2 nanocomposite loaded on the activated carbon [38] and $Cu(OH)_2$-NP-AC [39] as the adsorbents respectively. Saad et al. and Sharifpour et al. carried out investigations on CV dye adsorption using polyaniline nanoparticles (PANP) [40] and Sn (O, S)-NPs –AC [41] and observed a fast adsorption rate and rapid attainment at equilibrium condition, reveals the ultrasonic efficiency in wastewater treatment.

This research work aims (i) to superficially synthesise nanourchin structured α- MnO_2 (ii) to analyse the growth mechanism during the synthesis of the adsorbent (iii) to characterise the synthesised adsorbent (iv) to determine the efficiency of α- MnO_2 in the adsorption of CV and MB using ultrasonication and (v) to investigate the influence of different parameters - adsorbent dosage, ultrasonication time, ultrasonic frequency, pH, ultrasonic power, initial concentration of dye, competitive ions, ionic strength and humic acid.

2. Materials and methods

2.1. Materials

The chemicals used for this adsorption study were of analytical grade. CV (M.W = 407.97 g/mol, λ_{max} = 594 nm), MB (M.W = 319.85 g/mol, λ_{max} = 664 nm), Ammonium persulphate ($(NH_4)_2S_2O_8$), Ammonium Sulphate $(NH_4)_2SO_4$ and Manganous sulphate ($MnSO_4{\cdot}H_2O$) were purchased from Nice Chemicals Pvt Ltd, India and used without further purifications.

2.2. Synthesis of α-MnO_2

0.02 mmol $MnSO_4{\cdot}H_2O$, 0.08 mmol $(NH_4)_2SO_4$ and 0.02 mmol $(NH_4)_2S_2O_8$ were added to 70 mL of distilled water for the preparation of α-MnO_2 nanourchins. The prepared solution was transferred to a Teflon-lined stainless steel autoclave of 100 mL capacity. A brown-black product was obtained when the resulting homogeneous mixture was kept at 140 °C over 12 h. It was then filtered in Whatman #41 and washed many times using distilled water in order to remove residual ions. Then it was kept for overnight drying at 80 °C and calcinating for 3 h at 200 °C in the air [42].

2.3. Characterisation of α-MnO_2

At zero point charge, the pH on the surface of α-MnO_2 was determined by batch equilibrium method [43]. The initial values of pH were adjusted to the range of 2–10.5. This was done by adding H_2SO_4 or NaOH to 20 mL of distilled water. To each of these solutions, 0.003 g of α-MnO_2 was added. The resulting solutions were then continuously stirred by keeping in an orbital shaker at room temperature for 24 h. Whatman #41 filter paper was used to filter the solution and then measured the respective pH of the dye solutions. The graph for pH_{final} vs. $pH_{initial}$ was plotted and the intersection point of the bisector was taken as pH_{pzc} [44].

The nanourchins were characterised using Transmission Electron Microscopy (TEM-FEI Tecnai G2 T20 S Twin) as well as Scanning Electron Microscopy (SEM – Carl Zeiss, EVO 18) for their surface morphology and size. The X-ray photoelectron spectroscopy (Kratos Analytical, Axis Ultra) was used to determine the elemental composition of the nanourchins. Brunauer-Emmet-Teller (BET) analysis was conducted to determine the adsorbent surface area using a Quantachrome ASIQwin surface analyser. The crystallography was determined using X-ray diffraction (XRD – Bruker, D8 Advance). The functional groups' variation before and after adsorption of dyes, was analysed using FTIR spectrometer. The variations in the chemical and physical properties of the adsorbent were studied using Thermogravimetric analysis (TGA; TA instruments SDT–Q600) curve.

2.4. Preparation of dye solution

1 g of CV and MB were separately dissolved in 1 L of distilled water at a room temperature of (25 °C ± 2 °C) to obtain the stock solution. Then, the prepared solution was diluted to the required concentrations to obtain the adequate test solutions. Initial dye concentration was determined using a UV–visible spectrophotometer [45].

2.5. Adsorption protocol

Under ultrasonication (Elmasonic P300H ultrasonic bath, continuous mode, 80 kHz), continuous set of batch adsorption tests were performed to determine the adsorption capacity of α-MnO_2 for the effective removal of both the dye. Primary tests were carried out in the pH limits ranging from 2 to 10.5 for optimising pH. At the optimised pH value, experiments were performed in order to determine the influence of time for ultrasonication (3–15 min), adsorbent dosage (0.001–0.007 g/50 mL for CV and 0.001–0.01 g/50 mL for MB) and initial concentrations of dyes (50–150 mg/L). The dye samples were collected and the removal efficiency was estimated using an UV–Visible spectrophotometer. The obtained results were validated using kinetics as well as isotherms. The percentage of dye removed was computed from the Eq. (1).

$$\%dyeremoval = \frac{C_0 - C_e}{C_0} \times 100 \tag{1}$$

where 'C_0' is the initial concentrations of both the dyes (mg/L) and 'C_e' is the concentration of dyes at equilibrium (mg/L) which is depicted in the relation (Eq. (2))

$$q = \frac{v(C_0 - C_e)}{M} \tag{2}$$

The quantity of dye adsorbed q (mg/g), volume v (L) of the dye solution and dry weight of the adsorbent M (g) were calculated from the equation (Eq. (2)) [45].

2.6. Adsorption isotherms

The general purpose of adsorption isotherms at equilibrium is to understand and design the prevailing interaction mechanism between the adsorbate and the adsorbent [46]. In this study, for the initial concentration of 100 ppm, the isotherm studies were conducted for CV and MB. The adsorption capacity of CV and MB dye on α-MnO_2 were observed for various adsorption models like Langmuir, Freundlich and Temkin and the constants of each model were estimated.

2.6.1. Langmuir isotherm

A monolayer adsorption of CV and MB dyes on the α-MnO_2 surface occurs in the Langmuir isotherm model. The expectation is that no further adsorption happens on the adsorbate site if the dye molecule is covered at once. It is also assumed that these sites are having equivalent energies [47]. Irving Langmuir developed the equation as

$$\frac{C_e}{q_e} = \frac{C_e}{q_m} + \frac{1}{K_a q_m} \tag{3}$$

$$\frac{1}{q_e} = \frac{1}{q_m} + \frac{1}{C_e K_a q_m} \tag{4}$$

Here C_e (mg/L) represents the quantity of CV and MB dye adsorbed per unit mass of α-MnO_2 at equilibrium, q_m (mg/g) represents the maximum dye adsorption rate, q_e (mg/L) the quantity of CV and MB dye that is adsorbed per unit mass of adsorbent and K_a (L/mg) denotes the adsorption energy constant.

Separation factor (R_L) was associated to find the characteristics of the Langmuir isotherm (Eq. (5))

$$R_L = \frac{1}{1 + K_a C_0} \tag{5}$$

The adsorption behaviour of the adsorbate onto the adsorbent can be found by R_L. The R_L value greater than 1 and less than 0 represents irreversible adsorption, R_L equal to 1 represents linear whereas R_L greater than 1 shows unfavourable adsorption.

2.6.2. Freundlich isotherm

A heterogeneous surface adsorption is assumed to occur in the Freundlich isotherm model. A broad range of adsorbate concentrations can be provided in this model. The distribution of the heat of adsorption is non-uniform on the surface of the adsorbent. As per the given equation (Eq. (6)), the Freundlich isotherm was adapted for the sorption of both the dye onto α-MnO_2.

$$\log q_e = log K_f + \frac{1}{n}\log C_e \tag{6}$$

Here C_e (mg/L) represents the concentration of the CV and MB dye and q_e (mg/L) is the amount of CV and MB dye that is adsorbed per unit mass of α-MnO_2. n andK_f (mg/g) are the Freundlich constants associated with the adsorption intensity and the adsorption capacity per unit mass of the adsorbent respectively.

2.6.3. Temkin isotherm

The heat of adsorption is increasing linearly with coverage for all the molecules is the hypothesis in the Temkin adsorption model [47]. The linear form of this model is given by (Eq. (7))

$$q_e = BlnA_T + BlnC_e \tag{7}$$

$$B = \frac{RT}{B_T} \tag{8}$$

Here q_e (mg/L) is the amount of CV and MB dye that is adsorbed per unit mass of α -MnO_2, B is the Temkin isotherm energy constant, A_T is the equilibrium binding constant, B_T is Temkin constant, R represents universal gas constant and T is the temperature (K).

2.7. Adsorption kinetic studies

The controlling mechanism, as well as the adsorption rate, can be unstated from the rate constant study. The adsorption kinetics of the dyes on α-MnO_2 was examined by employing Lagergren's first-order kinetics, pseudo-second order, Elovich and Intra-particle diffusion model.

2.7.1. Lagergren's first-order kinetics

To determine the rate constants and the order of the ongoing process, Lagergren's first-order kinetics were employed for the adsorption of the dyes (MB and CV) onto α -MnO_2. The equation for this model is given by the (Eq. (9))

$$\log(q_e - q_t) = log q_e - \frac{k_1 t}{2.303} \tag{9}$$

where q_t and q_e are the quantity of CV and MB dye that is adsorbed at time t and at equilibrium respectively.

2.7.2. Pseudo-second order kinetics

The behaviour of adsorption all over the range is found out by employing Pseudo-second order kinetic model. The linear relation can be illustrated as following equation (Eq. (10))

$$\frac{t}{q_t} = \frac{1}{k_2 q_e^2} + \frac{t}{q_e} \tag{10}$$

$$h = k_2 q_e^2 \tag{11}$$

q_t and q_e are the quantity of CV and MB dye that is adsorbed at time t

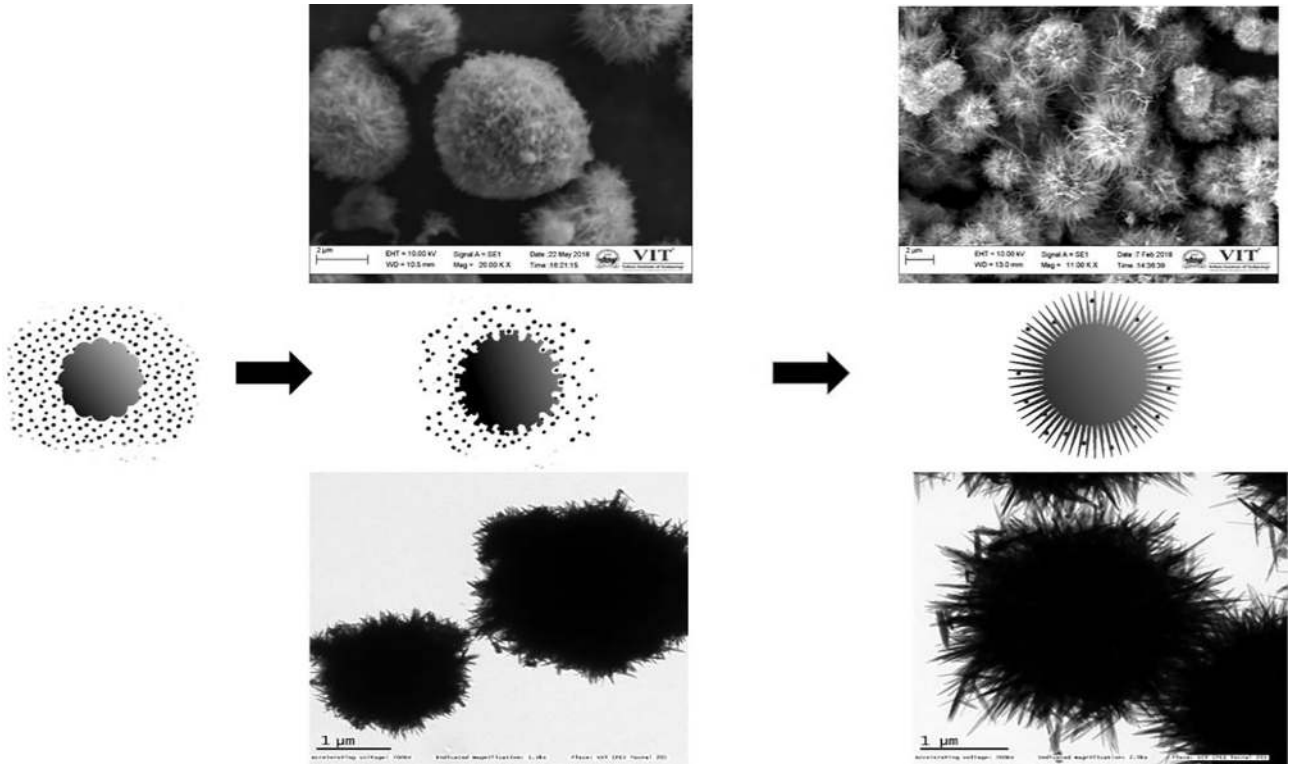

Fig. 1. Growth mechanism of α-$MnO_2$with respect to SEM and TEM.

and at equilibrium respectively. Here h (mg/g min) is the initial adsorption rate and expressed as in (Eq. (11)), k_2 is the rate constant for this model (g/mg min).

2.7.3. Elovich model

Chemisorption kinetics with a heterogeneous surface is mainly dealt with the Elovich model [48]. The linearized equation of the Elovich kinetic model can be expressed by Eq. (12).

$$q_t = \frac{1}{\beta}\ln(\alpha\beta) + \frac{1}{\beta}lnt \tag{12}$$

Here q_t (mg/g) is the quantity of CV and MB dye adsorbed at time t, α (mg/g/min) represents the initial adsorption rate and β is the chemisorption activation energy and the extent of surface coverage.

2.7.4. Intra-particle diffusion model

The adsorbate is assumed to be initially transferred on to the surface which is then transported to the available sites by a diffusion process in this model. The formation on a boundary layer is finally followed by the interaction of adsorbent within the sites [49]. The adsorption mechanism on CV and MB dye on α -MnO_2 was investigated by employing the intra-particle diffusion model. It is proposed that the adsorption of adsorbent (CV and MB) on adsorbate (α-MnO_2) varies proportionally to $\sqrt{t}$. Webber and Morris [50] stated the intra-particle diffusion equation as (Eq. (13))

$$q_t = k\sqrt{t} + c \tag{13}$$

where, q_t (mg/g) is the quantity of CV and MB per unit mass of α -MnO_2 at time t, and k (mg/g/$min^{1/2}$) is the intra-particle diffusion constant. The thickness of the boundary layer is given by the constant c (mg/g).

2.8. Error analysis

The best fitting isotherm and kinetics models were determined from the experimental data by the coefficient of correlation (R^2). The calculated q_e (q_{ecal}) values were estimated with the linearized equations of each model for kinetics as well as isotherms. The experimental, as well as the calculated data, were fitted into various error analysis functions like *ARE*, *MPSD*, *SD* and the smallest value indicating least error is determined.

The equations used for the error analysis are as follows [51]

$$ARE = \frac{100}{n}\sum_{i=1}^{n}\left|\frac{q_{emeas}-q_{ecal}}{q_{emeas}}\right| \tag{14}$$

$$MPSD = 100\sqrt{\frac{1}{n-p}\sum_{i=1}^{n}\left[\frac{q_{emeas}-q_{ecal}}{q_{emeas}}\right]^2} \tag{15}$$

$$SD = \sqrt{\sum_{i=1}^{n}\left[\frac{q_{emeas}-q_{ecal}}{q_{emeas}}\right]^2\frac{100}{n-1}} \tag{16}$$

3. Results and discussions

3.1. Growth mechanism of α-MnO_2

As per the observations made on the evolutions of crystallinity and morphology, the growth mechanism of α-MnO_2 nanourchins was rationalised. The α-MnO_2 synthesis mainly depends on the reaction between Manganese sulphate and Ammonium persulphate. The chemical reaction is represented as follows [52,53]:

$$Mn^{2+} + S_2O_8^{2-} + 2H_2O \rightarrow MnO_2 + 4H^+ + 2SO4^{2-} \tag{17}$$

$$MnSO_4 + (NH_4)_2S_2O_8 + 2H_2O \rightarrow \alpha{-}MnO_2 + (NH_4)_2SO_4 + 2H_2SO_4 \tag{18}$$

In the solution, the redox reaction occurring between $S_2O_8{}^{2-}$ and Mn^{2+} results in the production of basic units of MnO_2 within a short period of time. Development of α-MnO_2 nanourchins depends on the concentration of MnO_2 units within the solution. The proposed growth process is as shown in Fig. 1. Initially, the concentration of MnO_2 units in the solution is assumed to be very high. These units combine together

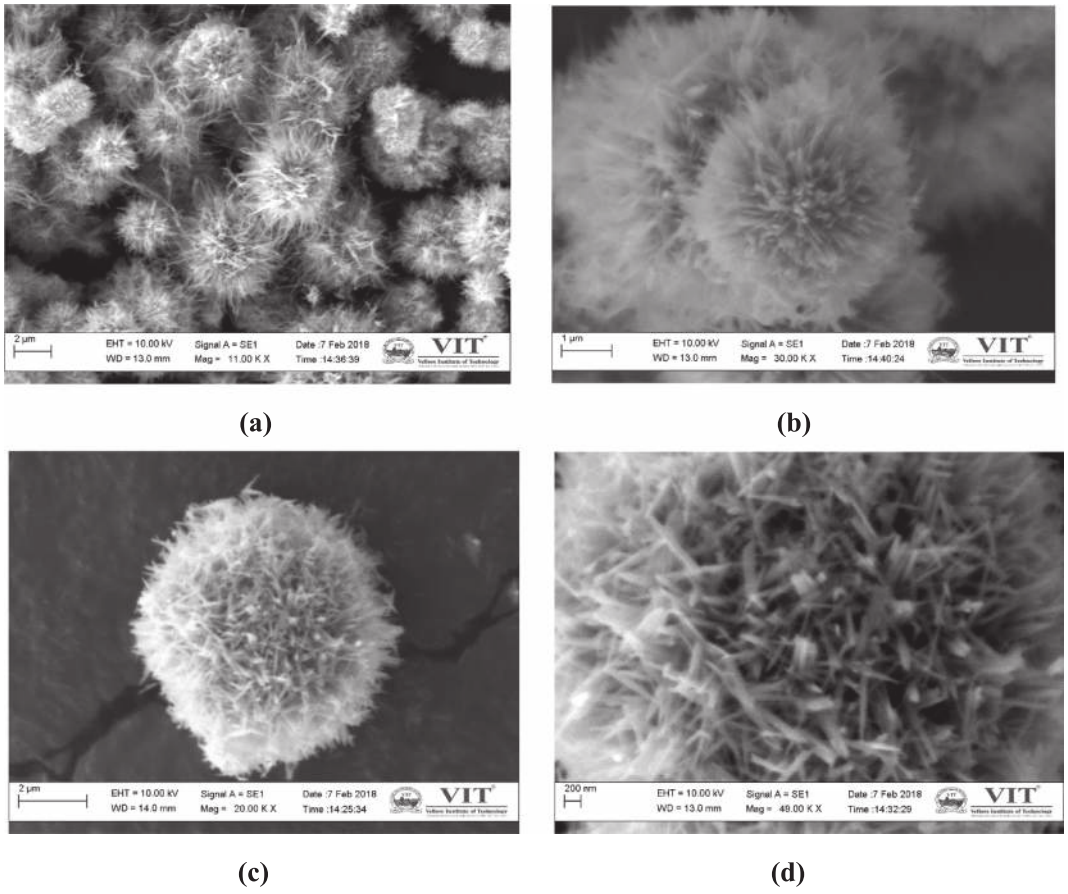

Fig. 2. (a–d) SEM images of α-MnO_2 at different magnifications.

to form a spherical shape which minimises the entire system energy [52]. The concentration of MnO_2 units in the solution decreased as these units were continuously transformed into a spherical shape. The whole system attains a thermodynamically stable environment as the concentration of these units were below a specified limit. From this, α-MnO_2 nanoneedles started growing to their one-dimensional growth habit [54]. The nucleation seeds represent the outer most surface in the growth mechanism where the growth of ultrathin nanoneedles became faster resulting in urchin-like structure.

3.2. Characteristics of α-MnO_2

The morphology of α-MnO_2 sample was determined using SEM analysis as represented in Fig. 2(a–d). Fig. 2d depicted that this sample has Urchin-like flower structure consisting of numerous nanoneedles with a thickness of various nanometers. These well-defined nanoneedles are observed with a size of 2 μm. Similar results were obtained by Zhou et al. [52] TEM analysis confirmed that the α-MnO_2 sample contains flower-like structures with a diameter of about 100 nm–200 nm. The close observation of TEM images emphasis the interconnectivity of nanoneedles with minute thickness (Fig. 3a). Nanourchin contains radially grown 1D nanoneedles of diameter less than 20 nm which is shown in Fig. 3b. This was in good concurrence with SEM analysis. The α-MnO_2 shows a single crystallite confirmed by the SAED (Selected Area Electron Diffraction) pattern with planes (110), (200), (220), (310), (400), (330), (420), (301), (510) and (411) (Fig. 3c). The TEM image shows a nanoneedle with interplanar spacing 0.214 nm, corresponding to the plane (400) of α-MnO_2 (Fig. 3d) [55].

The crystallinity and purity of the synthesised α-MnO_2 were identified using XRD [56]. Fig. 4 represents some broad peaks as well as sharp peaks. MnO_6 octahedral units form the basic structural arrangement of MnO_2 that were connected in various means to develop the crystallographic form. 1D, 2D and 3D tunnel structures were formed as the edges and vertices of octahedral units of MnO_6 were shared in various ways. Numerous octahedral subunits (n × m) formed from the size of the tunnel were used to describe various crystallographic forms [57]. The broad diffraction peaks are due to the presence of definite types of arbitrary intergrowths of pyrolusite (1 × 2 tunnel structure) and ramsdellite (1 × 2 tunnel structure) in MnO_2. These observations are made as per the "De Wolff model" issued in the year 1959 [58]. The diffraction peak at 2θ = 12.6°, 17.98°, 28.5°, 41.7°, 49.7°, 55.9°, 59.9° and 65.3° with the planes (110), (200), (310), (301), (411), (600), (521) and (002) in the spectrum can be well observed as α-MnO_2 (JCPDS No. 00-044-0141). Similar results were obtained by Shinde et al., and Thanh et al. [59,60]. The cell volume of α-MnO_2 is 274.1 $Å^3$. The obtained value is identical with the standard cell volume of 274.03 $Å^3$ [61] and the lattice parameters of tetragonal α-MnO_2 are a = 9.78 Å, b = 9.78 Å and c = 2.86 Å. Similar results were obtained by Shinde et al. [59]. The average size of the nanourchin MnO_2 crystal grains were observed as 14.33 nm from the Scherrer equation $D = K\lambda/\beta Cos\theta$ using the strongest diffraction peak (310) where K is the Scherrer constant (0.89), D is the crystal grain size (nm), λ is the X-ray wavelength (0.154056 nm) for Cu Kα, θ is the angle of diffraction peak and β is the full width at half maximum (FWHM) of the peak (310) whereas the diameter measured for nanourchin MnO_2 was 14.55 nm. Since the calculated and measured value of nanourchin MnO_2 is identical, it can be concluded that the results of TEM analysis and XRD are in agreement with each other.

The α-MnO_2 spectrum comprises two superimposed crystalline MnO_2 forms (Fig. 5a) [62]. A strong, as well as a weak band, were observed at 660.73 cm^{-1} and 553.57 cm^{-1} respectively in the IR spectrum. These strong bands and weak bands were in accordance with

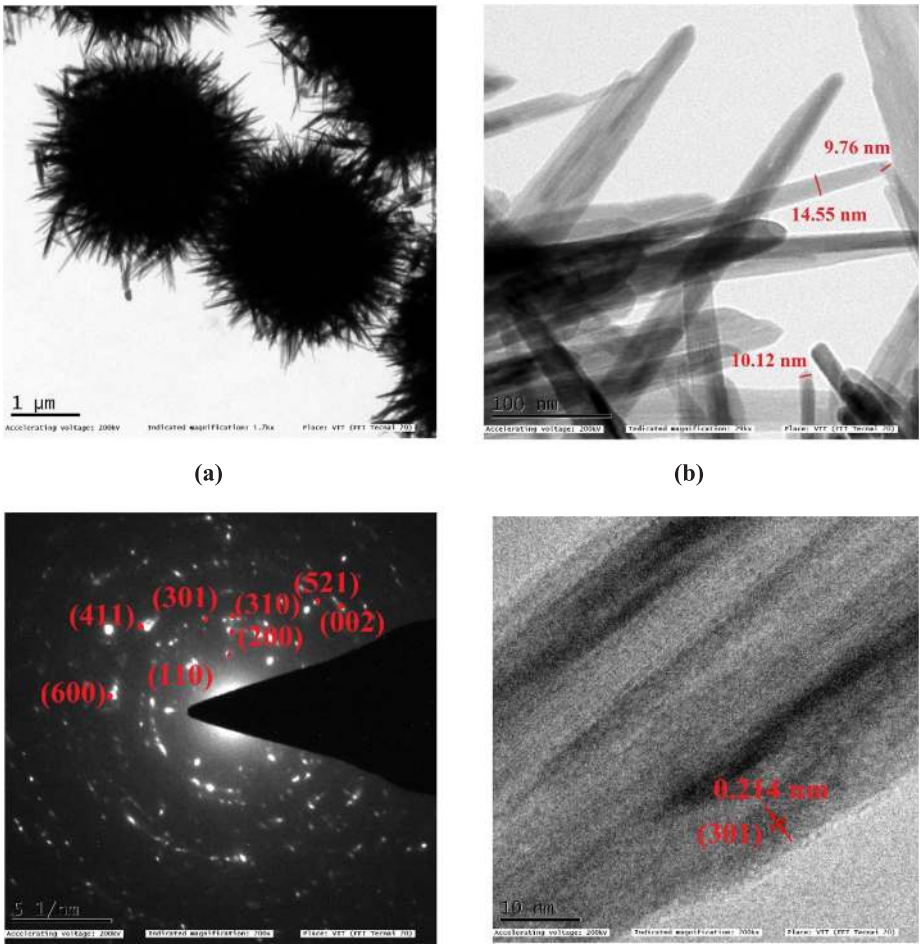

Fig. 3. (a),(b) TEM images at different magnifications; (c) SAED image of α-MnO_2 and (d) Interfringe distance ofα-$MnO_{24.}$

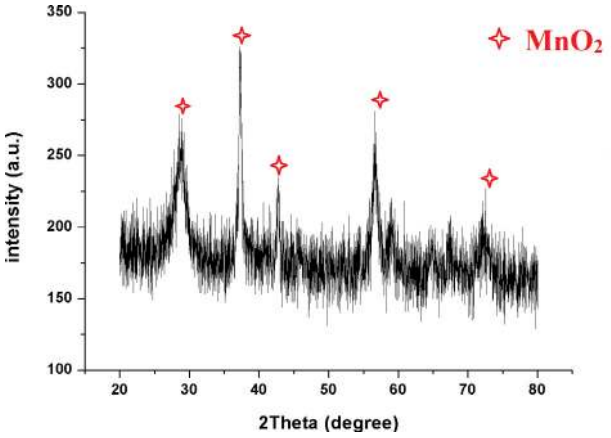

Fig. 4. XRD pattern of α-$MnO_{2.}$

the earlier details about R-MnO_2 [63]. The peak observed at 553.57 cm^{-1} was attributed to the vibration of Mn-O. Matsuo and Nakano [64] demonstrated that the oxides of rare earth and transition metals were characterised by an intense vibration mode. The peak for MnO_2 was located at 700.16 cm^{-1}. The bands observed at 700.16, 553.57, 495.71 and 455.20 cm^{-1} belonged to ramsdellite and the bands at 660.73 cm^{-1} attributed to the spectrum of pyrolusite [64]. The characteristics peaks at 1654.92, 1581.63, 1340.53, 1298.09, 1165, 908.47, 817.82, 665.44, 555.50 and 468.70 cm^{-1} were found for the CV adsorbed nanourchin (Fig. 5b). Similarly, the peaks at 979.84, 667.37, 555.50 and 491.85 cm^{-1} were observed over MB adsorbed nanourchin (Fig. 5c).

XPS analysis was performed in order to determine the facile elemental species (O, Mn and C) present on α-MnO_2 and shown in Fig. 6a. As represented in Fig. 6b, the catalysts represented two dissymmetric peaks observed at 642.19 (Mn $2p_{3/2}$) and 654.01 eV (Mn $2p_{1/2}$). With respect to various oxidation states of Mn, two subpeaks were obtained as Mn $2p_{1/2}$ and Mn $2p_{3/2}$ peaks were decomposed. The sub-peaks observed at 641.8 (or 642) and 653.4 (or 653.6) eV were designated to $Mn^{3+}(2p_{3/2})$ and $Mn^{3+}(2p_{1/2})$ ions, respectively. The sub-peaks situated at 642.7 and 654.1 eV were designated to $Mn^{4+}(2p_{3/2})$ and $Mn^{4+(}2p_{1/2})$ ions, respectively [65–67]. The XPS spectra of O 1s is represented in Fig. 6c. This spectrum is segregated into three different regions and these regions are described as follows: (i) Binding energy (BE) in the limiting range of 530.7–529.3 eV is specified as O_{lat} (Mn−O−Mn bond), corresponded to lattice oxygen species; (ii) Binding energy in the range of 531.0–532.6 eV is denoted as (O_{sur}, Mn−OH bond), corresponding to surface-chemisorbed oxygen species; (iii) Binding energy in the limits of 532.6–534.0 eV is denoted as (O_{ads}, H−O−H bond), corresponding to adsorbed molecular water species [48–50]. From Fig. 6c, it is observed that O_{lat}, O_{sur} and O_{ads} are positioned at 529.8 ± 0.2, 531.6 ± 0.2 and 533.1 ± 0.3 eV respectively [65,68–70].

BET equation is represented by the Langmuir isotherm which is obtained from the following (Eq. (19)) [71]

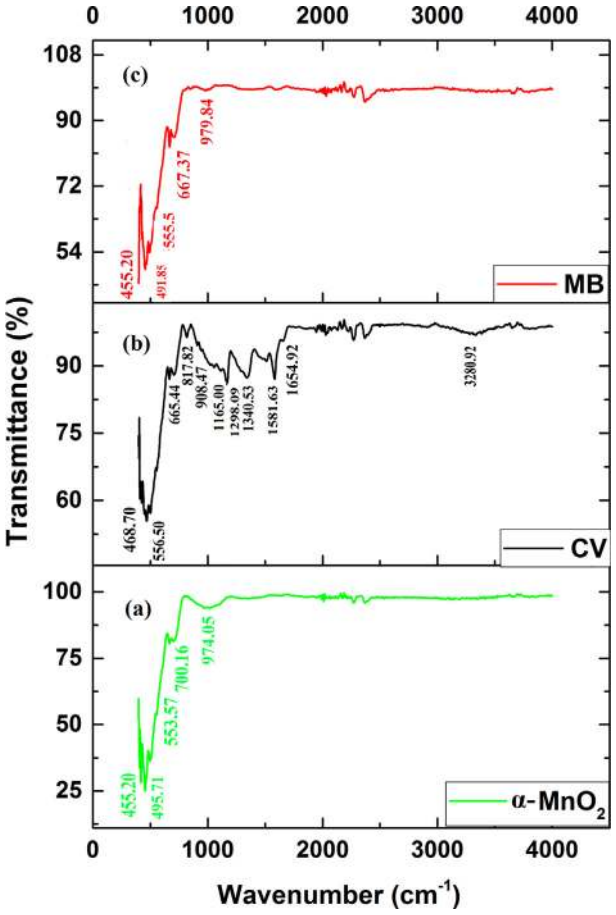

Fig. 5. FTIR spectrum of (a) α- MnO_2, (b) after adsorption of CV and (c) after adsorption of MB.

$$\frac{1}{V\left(\frac{P_0}{P}-1\right)} = \frac{C-1}{V_m C}\left(\frac{P}{P_0}\right) + \left(\frac{1}{V_m C}\right) \tag{19}$$

The plot for BET is a straight line which was plotted with $\frac{1}{V\left(\frac{P_0}{P}-1\right)}$ and $\frac{P}{P_0}$

The specific surface area and total surface area of the adsorbent was obtained from the following (Eq. (20)) [30,31]

$$S = \frac{V_m N_s}{V} \tag{20}$$

Fig. S1a represents pore volume and the BET line of α-MnO_2. For a time period of 6 h before use, the Quantachrome ASIQwin surface analyser was degassed for a temperature of 500 °C. 0.016 g of α-MnO_2 was has been used for the analysis along with the adsorbate as Nitrogen at −195.75 °C. Liquid Nitrogen was used for cooling under a pressure of 13.4 psi for a duration of 60 s of desorption and adsorption dwell time. A typical N_2 adsorption/desorption isotherm which is showed in Fig. S1b describes the characteristics of the mesoporous material. At lower relative partial pressures a small hysteresis loop was obtained which may be due to the presence of capillary condensation. At higher partial pressures, an intense rise in the nitrogen adsorption volume revealed the development of macro/mesopores due to the aggregation of particles [73]. The BJH analysis was used to establish the pore radius, that was determined as 10.99 Å. The cumulative adsorption surface area of α-MnO_2 was 51.51 m^2/g obtained from Barrett-Joyner-Halenda (BJH) having a total pore volume of 4.751 × 10^{-2} cc/g; with a radius less than 53.74 Å. From Fig. S1c, it was depicted that in the mesoporous range (2–50 nm diameters) contains greater than 90% of the pores and the rest (below 10%) were lying in the microporous range (less than 2 nm). Our results display that a large surface area is not played a significant role for high adsorption capacity, as is usually supposed, but instead large pore diameter and pore volume are primarily significant for effective and fast dye adsorption. Similar results were observed by Parker et al. using adsorbent which exhibits very high mesoporosity (above 80%), pore volume (above 1 cm^3/g) and pore diameter (between 14 and 19 nm), but with the surface area less than 300 m^2/g. On other hands when they used commercially available adsorbent (with high surface area and less than 20% mesoporosity), they achieved a low removal efficiency [74]. The determined values suggest the development of a mesoporous structure which is disordered and is found to be in accordance with the TEM images. The least amount of macro-pores are correlated to the gap between the aggregated particles. The average pore diameter was observed to be higher than the dimensions of MB- 1.38 × 0.59 nm [75]; CV −1.65 × 1.50 nm [76] dye molecules. Hence the adsorption of dye molecules increased due to the occurrence of substantial pore volume and mesoporous structures [72,73].

Nanourchins were heated from room temperature to 800 °C to perform the thermogravimetric analysis (TGA) (Fig. S2). This was carried out with a constant rate of 10 °C/min. In the beginning stage, a weight loss of 1.324% was observed at a room temperature of 180 °C as the moisture, coordinated water molecules and impurities were removed. In the second stage, a major weight loss of 4.205% was observed as the temperature was maintained at 180–400 °C. This was due to the losses in CO_2 as the $MnCO_3$ were transformed to tetravalent Mn^{4+} oxide (MnO_2) [77]. In the third step, the theoretical weight loss of 7.856% was observed as $MnCO_3$ was transformed to MnO_2 [77]. Complete decomposition of TGA analysis was performed at 800 °C on longtime air calculations. This was confirmed by the TGA of MnO_2 annealed at 800 °C and on air-annealing, the as-synthesised $MnCO_3$ was fully converted to MnO_2 [59].

3.3. Adsorption isotherms

The study on the adsorption isotherm model was conducted with the help of three models such as Langmuir, Freundlich and Temkin model to fit the constraints achieved from different experiments. The Langmuir constants q_m and K_a were given in Table 1. The graph between $1/q_e$ and $1/C_e$ was plotted with the slope $1/K_a q_m$ and intercept $1/q_m$ as shown in Fig. S3a. The adsorption of both the dyes (CV and MB) onto α -MnO_2 provided a linear line with the Langmuir model (R^2 = 0.9537 & 0.9611). The maximum rate of adsorption (q_m) for CV and MB were 5882.35 and 5000 mg/g respectively. Based on R_L value, CV and MB adsorption was favourable onto α-MnO_2. A graph of $\log q_e$ versus $\log C_e$ provided a linear line (R^2 = 0.9362 & 0.949) for CV and MB respectively with the slope ($1/n$) and intercept ($logK_f$) as shown in Fig. S3b representing Freundlich isotherm. The greater value of K_f (8.1767 & 6.8428) and n (1.177 &1.0927) denotes that the adsorption of the dyes on α -MnO_2 was favoured by heterogeneity and positive cooperativity binding [46]. The slope $1/n$ indicates the adsorption favorability and the value greater than 1 represents the favourable adsorption [49]. A plot between lnC_e versus q_e provided a linear line (R^2 = 0.8294 & 0.8142 from Table 1) for CV and MB respectively at each temperature with slope B and intercept $BlnA_T$ verifying the Temkin adsorption isotherm as shown in Fig. S3c. A greater value of R^2 was obtained for the Langmuir Type 2 isotherm and was acceptable to explain the adsorption of MB and CV on α-MnO_2. The monolayer adsorption is assumed in Langmuir isotherm in which no further adsorption takes place after attaining the equilibrium whereas heterogeneous surface adsorption is assumed in Freundlich, which is not restricting the formation of monolayer [47,49].

3.4. Adsorption kinetics

The rate of adsorption for the CV and MB removal was observed with kinetic models such as pseudo first-order, pseudo second-order,

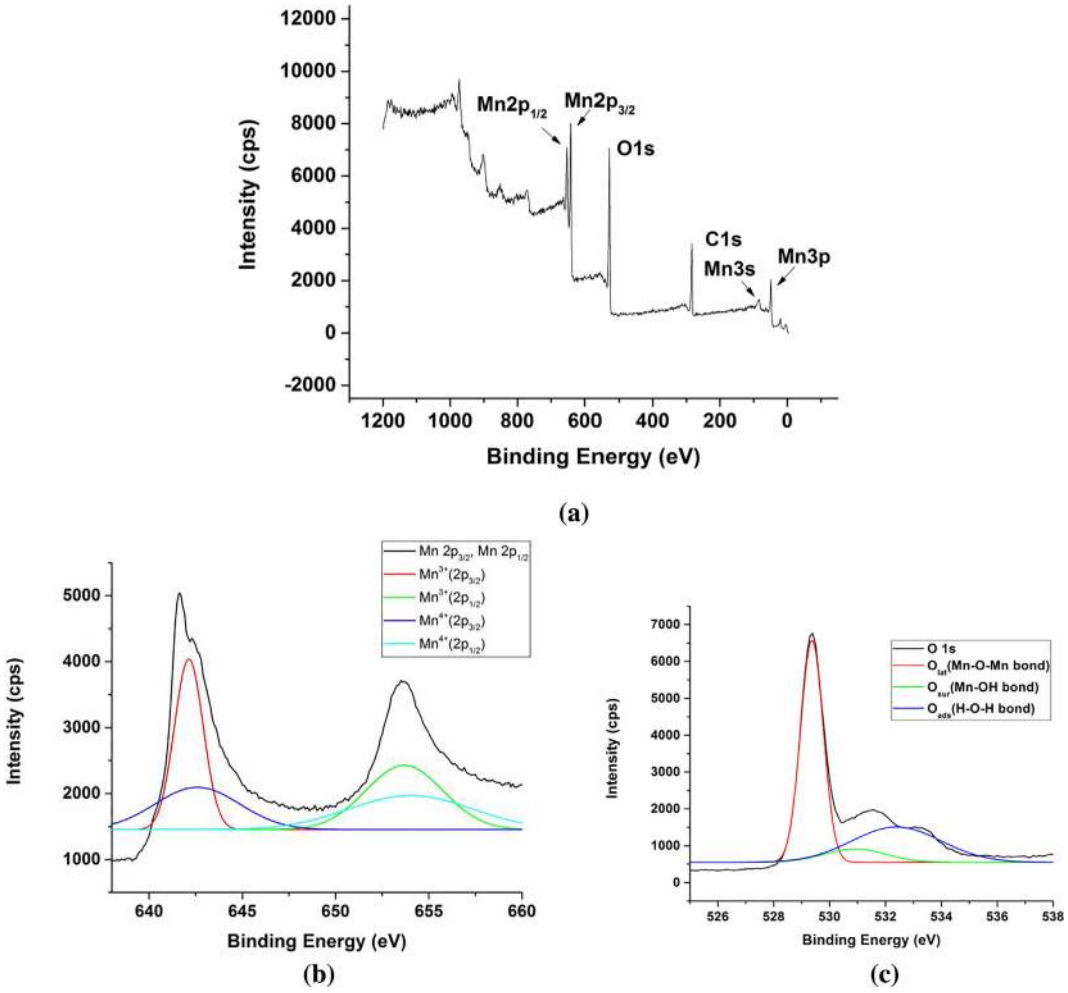

Fig. 6. XPS spectra of α-MnO_2 (a) Wide spectra, (b) Peaks corresponding to $Mn2p_{3/2}$, $Mn2p_{1/2}$ and (c) Peaks corresponding to O 1s.

Elovich and Weber-Morris intraparticle diffusion. For pseudo-first order kinetic model, the correlation coefficient (R^2) was observed as 0.9378 & 0.9678 for CV and MB respectively as shown in Table 2. k_1(L/min) represents the pseudo-first order rate constant which is obtained from the plot of $\log(q_e - q_t)$ versus t with slope $\frac{k_1}{2.303}$ and intercept $logq_e$ as shown in Fig. S4a. The constants q_e and k_2 can be determined from the slope $1/q_e$ and intercept $1/k_2 q_e^2$ of the line by plotting t/q_t versus$t$ as shown in Fig. S4b. The Eqs. (9) and (10), produces a straight line for pseudo-first order and pseudo-second order kinetics respectively. The correlation coefficient R^2 for both the kinetic models are given in Table 2. A higher value of correlation coefficient R^2 (0.9804 & 0.9955) was obtained for pseudo-second order was than Lagergren's first-order kinetics for CV and MB respectively. The q_e experimental values obtained were more close to the calculated value for the pseudo-second order than in pseudo-first order. In this adsorption, the chemical reaction seems substantial in the rate determining step. The pseudo-second order chemical reaction model is obtained as the best fit curve with a high correlation of the experimental data. The rate constants were severely influenced by ultrasonication process. A positive effect on the initial adsorption rate ($h = k_2 \times q_e^2$) was observed along with the higher rate constants. The value of h for MB (1624.32 mg/g/min) was higher than CV (1097.37 mg/g/min) indicates a faster adsorption rate in the initial stage of MB than CV on α -MnO_2. The monolayer adsorption of α-MnO_2 for CV and MB was not inclined due to ultrasonication. Without much variations in the adsorption capacity, we can conclude that ultrasonication has a positive influence on the speed to reach the equilibrium stage. Similar outcomes were observed by Bojic and Veljkovic [78], and Zhao et al. [79] for the ultrasonic-assisted dye adsorption. The adsorption mechanism seems to be chemisorption as it is chemically rate controlling [80].

The plot q_t versus lnt formed a linear line with a slope of $\frac{1}{\beta}$ and intercept of $\frac{1}{\beta}\ln(\alpha\beta)$ (Fig. S4c). The correlation coefficient (R^2 = 0.9462

Table 1
Langmuir, Freundlich and Temkin isotherms constants for the adsorption of CV and MB on α-MnO_2.

Langmuir				Freundlich			Temkin		
q_m (mg/g)	K_a (L/mg)	R_L	R^2	K_f (mg/g)	n	R^2	A_T (L/g)	B (J/mol)	R^2
Crystal Violet 5882.3	0.0181	0.3560	0.958	8.177	1.177	0.936	0.1672	1474.6	0.8294
Methylene Blue 5000	0.0161	0.3827	0.9611	6.8428	1.0927	0.949	0.1554	1310.5	0.8142

Table 2
Pseudo-first order, Pseudo-second order, Elovich and Intra-particle diffusion constants for the adsorption of CV and MB on α-MnO_2.

Dye (mg/L)	$(q_e)_{Exp}$ (mg/g)	Pseudo-first order			Pseudo-second order			Elovich			Intra-particle diffusion		
		$(q_e)_{cal}$ (mg/g)	k_1 (min^{-1})	R^2	$(q_e)_{cal}$ (mg/g)	k_2 (g/mg/min)	R^2	α (mg/g/min)	β (g/mg)	R^2	k_{ia} , k_{ib} (mg/g/$min^{1/2}$)	c_a, c_b (mg/g)	R_a^2,R_b^2
Crystal Violet													
100	3158.5	3471.36	0.259	0.937	3333.33	0.00011	0.9804	3475.22	0.0014	0.9462	688.08, 428.31	581.46, 1475.7	0.9692, 0.900
Methylene Blue													
100	3004	3786.16	0.484	0.967	3333.33	0.00018	0.9955	5639.09	0.0015	0.9487	924.79, 33.05	426.31, 2872.9	0.9913, 0.9819

& 0.9487) for CV and MB respectively was found and enumerated in Table 2. The diffusion rate constants for stage 1 and 2 is given by k_{ia} and k_{ib} (Table 2) respectively was acquired from the slope of the linear line of the plot q_t versus $\sqrt{t}$ (Fig. S4d). The line passes crossing the origin indicates that the rate limiting step is due to the intra-particle diffusion [50]. A multi-linear profile was formed with the line not crossing the origin indicating that the boundary layer diffusion also participates in the adsorption of CV and MB dye on α -MnO_2. Addition to that, the intra-particle diffusion of the CV and MB occurs in two stages. The initial stage represents the macro-pore diffusion (phase I) and the latter stage represents the micro-pore diffusion (phase II). These constants k_{ia} and k_{ib} are given in Table 2. Thus the result implicates that the adsorption of both the dyes on α -MnO_2 involves more than a single stage. In the initial stage, the fitting line did not cross the origin, depicting the resistance of the boundary layer in the adsorption. The intercept (Table 2) value for both the dyes was found to be less with a sharp rise. In the latter stage, the deviation of the fit line was detected, illustrating the difference in mass transfer with time in the initial and the second stage. The adsorption is controlled by the intra-particle diffusion model where the rate determining step during the process was intra-particle diffusion as the k_{ib} value for the second stage is smaller than the k_{ia} value for the second stage. The increased value of k_{ia} in both the dyes in the initial stage indicates that the mass transport happens into the pores by the generation of turbulence due to ultrasonication. The model represents the pore diffusion is not only the sole rate determining step but also bulk diffusion and intra-particle diffusion plays an important role in the initial and the latter stage of the adsorption. The boundary layer thickness values (Table 2) c_a and c_b increased after the initial stage in both adsorption of CV and MB dye on α-MnO_2 is given in Table 2. The higher value of c in the latter stage indicates more intercept value, thus increase in the boundary layer thickness.

It is found by comparing the errors for all the above models were compared that ARE model gave the least error for Langmuir isotherm and pseudo-second order kinetics for CV as well as MB. Thus it can be concluded that the Langmuir isotherm as well as the pseudo-second order models signifies the experimental data and is the best representation for the adsorption in this study. Several error analysis models for isotherm and kinetics were conducted. The results concluded that ARE model gave the least error for Langmuir isotherm and pseudo- second order kinetics for CV as well as MB is shown in Table S1. Also, a comparison study was conducted from previous papers on the adsorption of different dyes onto the adsorbent MnO_2 (Table 3).

The identification of mechanism behind the adsorptive removal of CV and MB is an important exercise. The experimental results of various pH and point of zero charge show that the electrostatic interaction played an important role during the adsorption process. In addition, the high mesoporosity nature of α-MnO_2 nanourchins played a significant role in the removal process. Also, the results indicate that the adsorption process is quick and approaches its equilibrium in 15 min. This behaviour could be attributed to the filling up of the active unadsorbed sites because of ultrasonic assistance. In overall, it is proposed that the combined effect of electrostatic attraction, the presence of high mesoporosity and ultrasonic assistance helped in the adsorptive removal of CV and MB.

3.5. Effects of various parameters on adsorption of dyes

3.5.1. Effect of pH

UV–visible spectrum for the dyes MB and CV in the visible region shows a main peak of maximum absorbance at an optimum concentration of 100 ppm and λ_{max} at 664 nm and 594 nm respectively as shown in Fig. S5(a, b). These results show that the spectrums of both the dyes were not affected by the variation in pH from 4 to 10. The obtained spectrum was in agreement with the previous studies reported by Jihane et al. and Xuegang et al. [81,82]. Hence all the experiments were performed in those stable pH ranges.

Oxides of Manganese are basically Lewis acids. They deprotonate for various values of pH [83]. As a result, the surface of these oxides possesses net positive as well as negative charge below and above respectively in point of zero charges (pH_{pzc}). The positive charges have a tendency to attract negative charges and vice versa due to the electrostatic force of attraction which leads to adsorption after $pH_{pzc,}$ which is 5.6 (Fig. S5c). Thus complex formation becomes one of the mechanisms for removal of the adsorbate which are CV and MB dyes. The adsorption of MB and CV occurs after pH_{pzc} of α-MnO_2. The resultant complex compounds' formation on the surface of the adsorbent is due to the electrostatic force of attraction between α-MnO_2 and respective dyes [84].

The adsorption capacity of α-MnO_2 on CV was observed and it was inferred that the minimum removal efficiency was obtained at pH 4 which was 54.76% and at pH 10 the removal efficiency of 90.37% was obtained that was found to be maximum. This depicts that, for the

Table 3
Half-life and half-capacity concentration for the ultrasonic assisted adsorption of various dyes on to various adsorbents - A comparison from previous literature studies.

Dyes	C_0 (mg/L)	Adsorbents	q_m (mg/g)	K_a (L/mg)	$C_{e,1/2}$ (mg/L)	q_e (mg/g)	k_2(g/(mg min))	$t_{1/2}$ (min)	References
Methylene blue	100	α MnO_2	5000	0.0161	62.11	3004	0.00018	1.84	This work
Crystal violet	100	α MnO_2	5882.3	0.0181	47.16	3158.5	0.00011	2.87	This work
Congo red	200	α – MnO_2	625.00	4.50	0.22	283.29	2.72	0.0012	[36]
Acid green	60	– MnO_2	76.923	0.1048	9.54	0.938 ± 0.0125	0.256 ± 0.0914	4.16	[99]
Malachite green	40	Activated carbon MnO_2	90.909	0.0753	13.28	53.73	1.172×10^{-3}	15.88	[100]

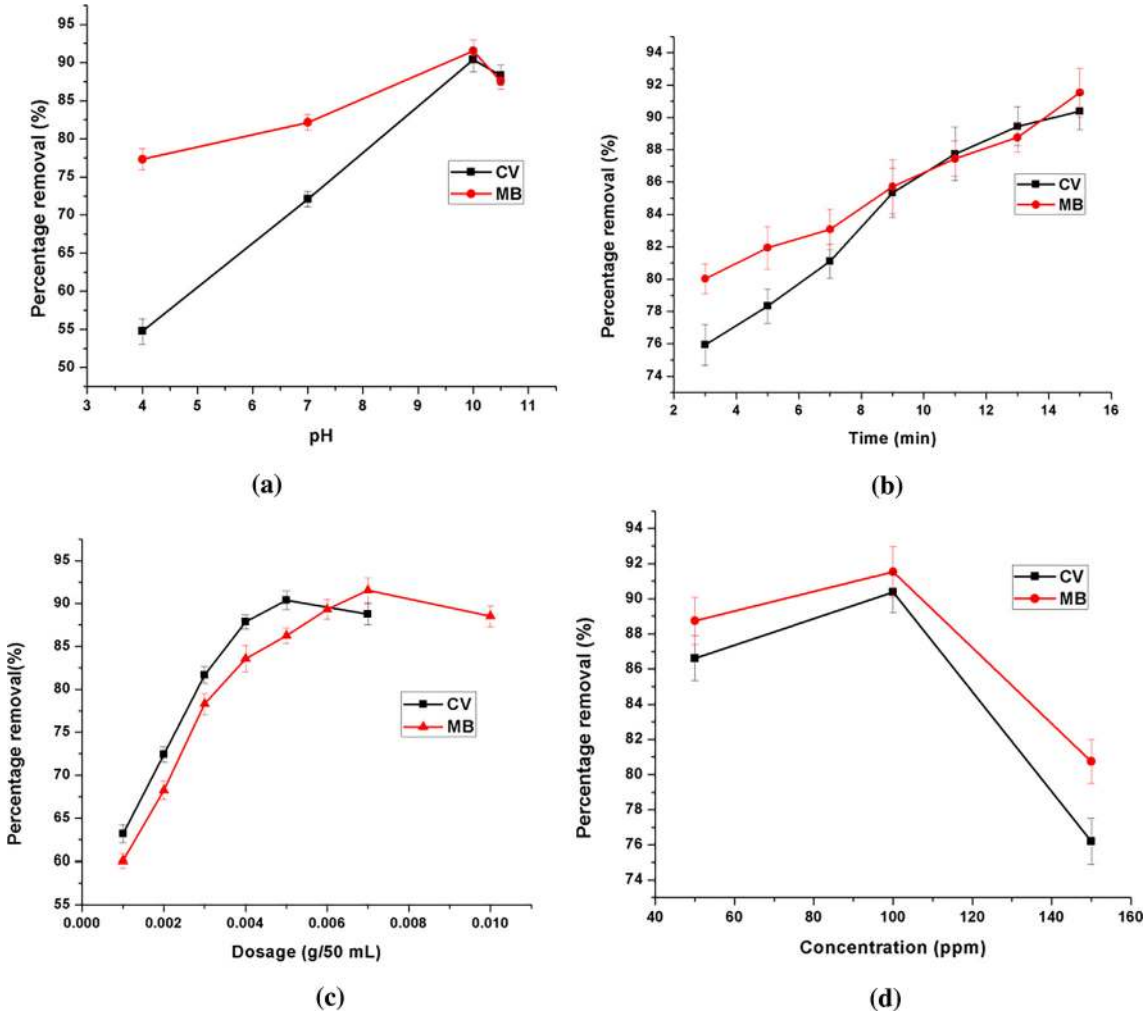

Fig. 7. Effect of (a) pH; (b) sonication time; (c) adsorbent dosage and (d) initial dye concentration on CV and MB adsorption.

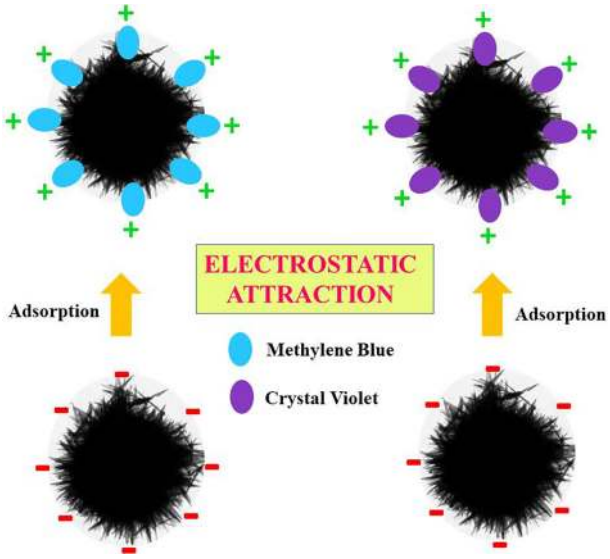

Fig. 8. Proposed electrostatic attraction of CV and MB adsorption onto α-MnO_2.

removal of the dye, initial pH plays a significant role. The difference in the adsorption capacity may be due to the dipolar attraction of CV molecules. Similarly for MB, at pH 4 the removal efficiency was minimum i.e. 77.32% and the maximum removal efficiency of 91.54% was observed at pH 10. From this, it can be inferred that the surface of the binding sites is being influenced by varying pH (Fig. 7a). Fig. 8 shows the proposed mechanism for CV and MB adsorptive removal. The α-MnO_2 interacts with an aqueous solution as well as with dye molecules' degree of ionisation. The low removal efficiency at acidic pH values could be attributed to oxidation of dye molecules by α-MnO_2 via N-demethylation, not a pure adsorptive removal. Earlier studies confirm that the removal of Methylene Blue at acidic conditions using oxides of manganese led to oxidative cleavage of dye molecules via N-demethylation. Also, their result indicates the reduced adsorptive ability and increased oxidation capacity of the hybrid fibre at acidic conditions [33,85].

3.5.2. *Effect of ultrasonication time*

The influence of sonication time for the adsorption capacity of α-MnO_2 on CV and MB dyes were observed by collecting the effluents at various time intervals i.e 3, 5, 7, 9, 11, 13 and 15 min. The experimental results indicated that the adsorption capacity of α-MnO_2 increased as the ultrasonication time increased (Fig. 7b). This is because the mass transfer occurred in short sonication time, due to the presence of higher surface active sites which resulted in higher initial adsorption rate. For CV removal efficiency at 3 min and 15 min was 75.93% and 90.37% respectively. Similarly, for MB, the removal efficiency was 80.02% and 91.54% respectively.

3.5.3. *Effect of adsorbent dosage*

The effect of α-MnO_2 dosages on CV dye was observed by varying

dosages in 100 ppm dye solution from 0.001 g/50 mL–0.007 g/50 mL. The removal efficiency of CV increased from 63.17% at dosage 0.001 g/50 mL to a specific limit (0.005 g/50 mL) where the efficiency was 90.30% and then the efficiency decreases to 88.76% at 0.007 g/50 mL. Similarly the removal efficiency increased from 60.08% at 0.001 g/50 mL to 91.54% at 0.007 g/50 mL for MB at 100 ppm. Afterwards, the removal efficiency was decreased to 88.52% at 0.01 g/50 mL (Fig. 7c). The increase in the adsorption capacity was due to the presence of active spots on the surface of α-MnO_2 whereas the decrease in the adsorption capacity was due to the saturation of active sites of the adsorbent. At pH 10.5, the removal efficiency decreases for both the dyes which were 88.34% for CV and 87.57% for MB.

3.5.4. Effect of initial concentration of dyes

The effect of initial concentration of CV and MB dyes were observed by varying concentration from 50 ppm to 150 ppm of the dye solution. The removal efficiency of the adsorbent in case of CV increases from 86.62% to 90.37% with an increase in concentration from 50 ppm to 100 ppm and decreases to 76.2% at 150 ppm. Similarly, for MB, the removal efficiency increases from 88.75% to 91.54% with an increase in concentration from 50 to 100 ppm and decreases to 80.75% at 150 ppm (Fig. 7d). This is due to, at lower concentrations the surface area available is more so that the adsorbent surface occupies numerous dye particles. Therefore saturation of active spots of α-MnO_2 occurs resulting in a decrease of removal efficiency.

3.5.5. Effect of temperature

Temperature is a physiochemical factor that leads to the variation in the removal efficiency of α-MnO_2. The effects of temperature were investigated for the dyes CV as well as MB by varying temperature from 20 °C to 50 °C. Maximum removal efficacy for CV was obtained as 90.37% at 30 °C and for MB maximum removal efficacy of 94.82% was obtained at 50 °C (Fig. S6a). This could be attributed to the weakening of bonds between dye molecules and α-MnO_2 at different temperatures.

By using Van't Hoff equation, the thermodynamic parameters like a change in free energy ΔG, change in enthalpy ΔH and change in entropy ΔS can be determined, which influence adsorption of heat for adsorbate onto adsorbent as shown in Table 4.

$$K_d = \frac{q_e}{C_e} \tag{21}$$

$$\Delta G = -RT \ln K_d \tag{22}$$

$$lnK_d = \frac{\Delta S}{R} - \frac{\Delta H}{RT} \tag{23}$$

where T is the temperature, R is the Gas coefficient (8.314 J/mol/L), K_d is the distribution coefficient [83]. The thermodynamic parameters such as ΔH, ΔS were found using Eqs. (22) & (23), constraints $\ln K_d$ vs 1/T in linear regression analysis of the Van't Hoff plot (Fig. S6b). The negative ΔG values depict that the CV and MB dyes' removal were spontaneous and feasible [86]. The negative ΔH value (−56.136 KJ/mol) for CV adsorption indicates to be an exothermic process whereas positive ΔH value (39.0225 KJ/mol) for MB adsorption indicates to be an endothermic process. ΔS value is observed to be positive for the adsorption of MB representing an increase in the randomness at the solid/solution interface whereas the decrease in randomness observed in the MB adsorption, is represented by the negative ΔS value [47,86].

Table 4
Thermodynamics parameters for the adsorption of MB and CV onto α-MnO_2.

T(K)	ΔG (KJ/mol)		ΔH (KJ/mol)		ΔS (KJ/mol/K)	
	MB	CV	MB	CV	MB	CV
293	−2.225	–	39.025	−56.136	0.142	−0.143
303	−4.977	−11.44				
313	−5.539	−8.913				
323	−6.718	−8.614				

3.5.6. Effect of ionic strength on dye removal

The effect of ionic strength on CV and MB dyes removal by varying the concentrations of NaCl was studied. As the concentration of NaCl increases the removal efficiency of CV and MB dyes also increases i.e., as the concentration of NaCl increased from 0.1 to 0.4 mol/L, the adsorbent removal efficiency for CV increased from 90.71% to 94.56%. Similarly, with the same increase in NaCl concentration, the removal efficacy increased from 91.87% to 95.86% for MB dye (Fig. S7). This trend occurs due to the competitive adsorption of ions as well as molecules of the dyes [87,88].

3.5.7. Effect of competitive ions

The adsorption process was hindered by the inorganic cations present in the effluent from textile industries. For this reason, the effect of inorganic cations (Na^+, Mg^{2+} and Fe^{3+}) on the removal of CV and MB dyes were studied using ultrasonic-assisted adsorption process. The results were represented in Fig. S8. The CV and MB adsorption in the presence of cations was compared with the dye adsorption in the absence of cations. A slight reduction in the removal efficiency of CV and MB dyes were observed in the presence of Mg^{2+} was due to the competition of Mg^{2+} with dye molecules to adsorb on active sites of the α-MnO_2. The slight increase in adsorption of dyes in the presence of Na^+ was due to the surface bridging mechanism and complexes on active sites [89]. On the other hand, the presence of Fe^{3+} leads to the significant reduction in the removal efficiency of both the dyes which was due to its high tendency to adhere to the negatively charged adsorbent, resulting in the decrease in ion interaction on the surface of α-MnO_2 for adsorption of dyes [90].

3.5.8. Effect of humic acid

The effect of humic acid (HA) on the adsorption of dyes is shown in Fig. S9. An increase in the HA concentration increases the adsorption of CV and MB dye molecules onto the surface of α-MnO_2. This might be ascribed to the unsaturation of active sites available on the α-MnO_2. The high-affinity force between dye molecules and the α-MnO_2 was the reason for the faster uptake of dye molecules than HA. Also, at a higher HA concentration, the driving force of HA adsorption onto α-MnO_2 is weak to compete with the dye molecules. This depicts that the competitive adsorption of HA onto the α-MnO_2 was lesser than the dye molecules [91].

3.5.9. Effect of ultrasound frequency

The adsorption capacity of α-MnO_2 considerably increases as the ultrasonic frequency increases. The ultrasound frequency for CV and MB dyes were tested at 37 and 80 kHz. The removal efficiency was maximum at 80 kHz for both CV and MB dyes which were 90.13% and 91.33% respectively. This change can be described with respect to cavitation bubbles' collapse time and resonance size. The size of the cavitation bubble varies with changing ultrasonic frequency and the relation between ultrasound frequency and bubble radius can be expressed as the following (Eq. (24))

$$f = \frac{1}{2\pi r}\sqrt{\frac{3\gamma}{\rho}\left(P_0 + \frac{2\sigma}{a}\right) - \frac{2\sigma}{a\rho}} \tag{24}$$

where r is the resonant bubble radius, f is resonant frequency, is the ratio of heat capacities of gas at constant volume which is 1.39 for air and pressure P_0 is the ambient pressure. Density is assumed to be 1.0 g/cm^3, surface tension is ignored [92]. Free bubble resonance size is 40.6 μm at 80 kHz and 87.8 μm at 37 kHz as reported in our previous work (Table 5) [72]. The time of the collapse of bubbles decreases as the radius of the resonance bubble decreases, which is given by the following (Eq. (25))

Table 5
Changes in microbubble characteristics with different frequency [72].

Frequency (kHz)	r (μm)	A (μm^2)	V (nL)	A/V (μ/m)	τ (μs)
37	87.8	9.68×10^4	2.83	3.42×10^{-2}	8.03
80	40.6	2.07×10^4	0.28	7.39×10^{-2}	3.71

A and V represent the surface area and volume of a bubble, respectively.

$$\tau = 0.915r\sqrt{\frac{\rho}{P_m}}\left(1 + \frac{P_v}{P_m}\right) \tag{25}$$

where, P_v is pressure in the bubble at the beginning stage of collapse of the bubble, P_m is the pressure in the liquid [93]. The bubble collapse time 3.71 μs at 80 kHz and 8.03 μs at 37 kHz. At higher frequencies the acoustic cycles' growth is more and as the collapse time reduces the maximum size of cavitation bubbles decreases [93]. Acoustic cavitation has better efficiency when compared to conventional agitation. Increase in the adsorbent surface area is due to the dispersion of converging magnetic powders caused by the ultrasound. Larger bubbles have the tendency for intense collapse; they have more stability compared to smaller bubbles. During the adsorption process, cavitation bubbles that are stable and stays in equilibrium towards lower loadings may block the active sites [94].

3.5.10. Effect of ultrasonic power

Ultrasonic power becomes a vital factor in dye removal which determines the removal efficiency of an adsorbent. The effect of power was examined by varying it at 40, 70 and 100 W at 32 °C, for 37 and 80 kHz. The results depicted that at 70 W and 80 kHz, the maximum removal efficiency of 90.13% for CV and 91.33% for MB are obtained. The adsorption capacity of both the dyes also increases by 15 min sonication time. The enhancement in the number of cavities generated is owing to the increase in the magnitude of power dissipation of the horn, and hence the cumulative pressure pulse may also increase. The maximum rate of adsorption is obtained at the optimum value of ultrasonic intensity. When power increases from 70 to 100 W, the efficiency of removal decreases to 86.32% at 100 W, 80 kHz (Fig. 9). This is because of desorption of both the dyes at higher powers. When the ultrasound intensity crosses the required range minute gas bubbles get generated in the dye solution. This disperses the sound waves to the vessel walls and also to the transducer. Less amount of energy was only dissipated into the liquid when the vessel was exposed to higher powers. As a result, consumption efficiency reduces due to the decrement in adsorption capacity [83].

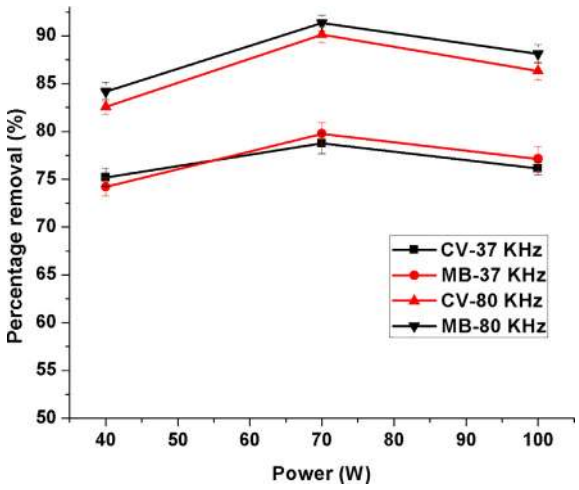

Fig. 9. Effect of frequency and power on CV and MB adsorption.

3.6. Half-life and half-capacity concentration

The solute equivalent equilibrium concentration ($C_{e,1/2}$) in liquid phase once it reaches the half of adsorption capacity ($q_e = 0.5q_m$) is derived from the Eq. (11) and is given as

$$C_{e,1/2} = \frac{1}{K_a} \tag{26}$$

From the above equation, it is clear that the half-capacity concentration ($C_{e,1/2}$) is the inverse of Langmuir constant K_a [95]. At the half-life $t = t_{1/2}$ of the adsorption process, q_t becomes $q_t = 0.5q_e$, in the adsorption process.

$$t_{1/2} = \frac{1}{k_2 q_e} \tag{27}$$

The above equation is derived from Eq. (17), replicates the physical importance of kinetic parameter in pseudo-second order model. In the adsorption process, half-time $t_{1/2}$ is inversely proportional to $k_2 q_e$ [95]. The values of half-life and half-capacity of CV and MB dye are shown in Table 3. The half-life ($t_{1/2}$) of CV and MB was obtained at 2.87 min and 1.84 min respectively. A minimum value is acquired reveals a faster rate of adsorption. Another substantial parameter is the half-capacity concentration. The $C_{e,1/2}$ of MB and CV adsorption was 62.11 mg/L and 47.16 mg/L respectively which is greater than all other dyes given in Table 3. This indicates that α-MnO_2 has the capacity to remove CV and MB at a higher level. It is important to link the kinetic parameters with operational experiment conditions. The values of k_1, k_2 and h were obtained at optimised (pH -10 for both dyes; C_i-100 mg/L for both dyes; adsorbent dosage - 0.005 g/50 mL for CV and 0.007 g/50 mL for MB) experimental conditions. As shown in Table 3 the values of q_m, half-capacity concentration, half-life and k_2 obtained from this research study has been compared with other research works. High half capacity concentration and low half-life values indicate rapid uptake revealing the promising capability of α-MnO_2 at a larger level.

3.7. Characteristic curves of adsorption

The adsorption characteristic curves were plotted using the Eq. (28), re-written from Eq. (27)

$$t_x = \frac{W}{k_2 q_e} \tag{28}$$

where $W = q_t/(q_e - q_t)$. At fractional adsorptions

$$X = q_t/q_e \tag{29}$$

And letwhere,

$$W = X/(1-X) \tag{30}$$

where $q_t/q_e = 1$, W = infinite and t_x = infinite at equilibrium.

For determining the best fit, linear squared regression correlation coefficient (R^2) were used [96].

As X = 1 and W reaches infinity, the relation between the variable of X values and fractional adsorption at any time was found. This is shown in Fig. S10. When W and t_x increases rapidly and W reaches 1, X value and t_x values are to be considered for making proper decisions. At the turning point of the curve, the value of t_x of adsorption is at X = 0.96. Time needed for various values of X are listed in Table S2. 1, 3, 5, 7, 9, 11, 13, 15 min are the values obtained for the adsorption of CV on α-MnO_2 at $t_{0.42}$, $t_{0.51}$, $t_{0.70}$, $t_{0.75}$, $t_{0.84}$, $t_{0.91}$, $t_{0.97}$, $t_{0.98}$. Similarly for the adsorption of MB, the values are 1, 3, 5, 7, 9, 11 min for $t_{0.46}$, $t_{0.64}$, $t_{0.84}$, $t_{0.95}$, $t_{0.98}$, $t_{0.99}$. For the operation time of CV; when the X value increases from $t_{0.42}$ to $t_{0.51}$, the percentage removal increases by 18.5% with 2 min increase whereas the removal efficiency increases by 26.84% for the same 2 min interval in operating time for $t_{0.7}$ and $t_{0.51}$. For the operation time of MB; when the X value increases from $t_{0.46}$ to $t_{0.64}$, the percentage removal increases by 29% with 2 min increase

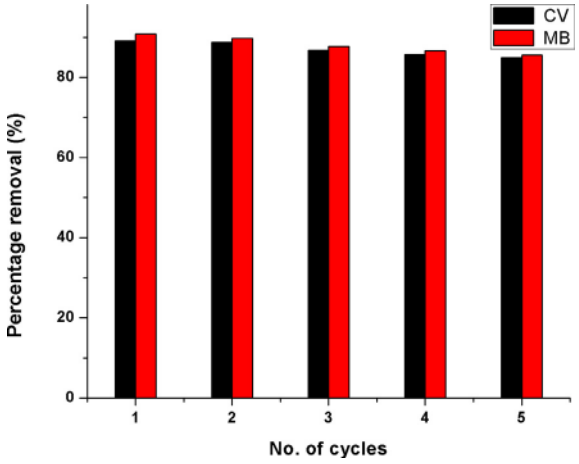

Fig. 10. Reusability study of α-$MnO_2$for five consecutive cycles.

whereas the removal efficiency decreases by 24% for the same 2 min interval in operating time for $t_{0.84}$ to $t_{0.64}$. The X values are decided for the better economic feasibility, with respect to the actual operating conditions.

3.8. Reusability of adsorbents

Regeneration of the adsorbents is considered as a vital evaluation index in measuring the potential of adsorbents' applications. The use of α-MnO_2 was separated after the sorption experiments by the process of centrifugation. 25 mL of 50% ethanol solution was mixed and shaken at 30 °C for a time of 15 min. The mixture was filtered using #Whatman 41 and dried in the oven at 70 °C [97]. The concentration of both the dyes was calculated after every recycling using UV–Vis spectroscopy. This process was continued for five times and thereby inferred that α-MnO_2 can be recovered as well as reused without significant reduction in mass (Fig. 10) The experiments depicted that 84.94% and 85.54% of removal efficiency was obtained for CV and MB respectively, even after five continuous cycles [98].

4. Conclusion

This study investigated the efficient removal of CV and MB by ultrasonic-assistance using an urchin like α-MnO_2 nanostructures synthesised by hydrothermal method. The synthesised nanourchins were characterised by XPS, SEM, XRD, FT-IR, TEM, BET and TGA to investigate the physico-chemical features of the adsorbent. Various isotherm and kinetic models were studied for the CV and MB adsorption and it was found that the best fit line was achieved for Langmuir and pseudo-second order models. Several error models were studied and those results concluded that ARE model gave the least error for the Langmuir isotherm and pseudo-second order kinetic model. Experiments were conducted to optimise different parameters like pH (i.e., for CV- pH 10; MB - pH 10), adsorbent dosage (CV- 0.005 g/50 mL; MB - 0.007 g/50 mL), initial dye concentration(CV- 100 mg/L; MB-100 mg/L) and sonication time (CV - 15 min; MB - 15 min). The removal efficiency of both the dyes increased when the ultrasonic power and frequency increased in the range 40 W–70 W and 37 kHz–80 kHz respectively. The negative ΔH value (−56.136 KJ/mol) for CV adsorption indicates to be an exothermic process whereas positive ΔH value (39.0225 KJ/mol) for MB adsorption indicates to be an endothermic process. A positive increase in the removal efficiency of both the dyes was influenced by the increase in the concentration of competitive ions and humic acid, indicates a deeper understanding of their interaction with multi-pollutant wastewater. And finally, the reusability characteristics of α-MnO_2 were studied and revealed the feasibility of recycling process after five cycles of adsorption. The obtained experimental results displayed that α-MnO_2 is a promising adsorbent for the efficient removal of CV and MB from textile wastewater.

Acknowledgement

The authors extremely thank Vellore Institute of Technology, Vellore campus, for their utmost help, by providing the needful facilities as well as infrastructure for carrying out the work.

Appendix A. Supplementary data

Supplementary data associated with this article can be found, in the online version, at https://doi.org/10.1016/j.ultsonch.2018.07.045.

References

[1] S. Farhadi, F. Siadatnasab, Copper (I) sulfide (Cu 2 S) nanoparticles from Cu (II) diethyldithiocarbamate: Synthesis, characterization and its application in ultrasound-assisted catalytic degradation of organic dye pollutants, Mater. Res. Bull. 83 (2016) 345–353.
[2] I.O.A. & O.S.B. Aderonke Ajibola Adeyemoa, Review Metal organic frameworks as adsorbents for dye adsorption: overview, prospects and future challenges, Toxicol. Environ. Chem., 94 (2012) 1846–1863. doi:10.1080/02772248.2012.744023.
[3] A.Z. Abdullah, P.Y. Ling, Heat treatment effects on the characteristics and sonocatalytic performance of TiO_2 in the degradation of organic dyes in aqueous solution, J. Hazard. Mater. 173 (2010) 159–167, https://doi.org/10.1016/j.jhazmat.2009.08.060.
[4] R. Vinu, G. Madras, Kinetics of sonophotocatalytic degradation of anionic dyes with nano-TiO, Environ. Sci. Technol. 43 (2009) 473–479, https://doi.org/10.1021/es8025648.
[5] S. Sara, A. Rehana, M. Hassan, Y. Junejo, N. Hussain, Z. Ali, Ultra-fast catalytic reduction of dyes by ionic liquid recoverable and reusable mefenamic acid derived gold nanoparticles, J. Hazard. Mater. 190 (2011) 1030–1036, https://doi.org/10.1016/j.jhazmat.2011.04.047.
[6] A. Asfaram, M. Ghaedi, K. Dashtian, G.R. Ghezelbash, Preparation and characterization of $Mn_{0.4}Zn_{0.6}Fe_2O_4$ nanoparticles supported on dead cells of *Yarrowia lipolytica* as a novel and efficient adsorbent/biosorbent composite for the removal of azo food dyes: central composite design optimization study, ACS Sustain. Chem. Eng. 6 (2018) 4549–4563, https://doi.org/10.1021/acssuschemeng.7b03205.
[7] E. Alipanahpour, M. Ghaedi, A. Asfaram, S. Hajati, F. Mehrabi, Preparation of nanomaterials for the ultrasound-enhanced removal of Pb 2 + ions and malachite green dye: chemometric optimization and modeling, Ultrason. Sonochem. 34 (2017) 677–691, https://doi.org/10.1016/j.ultsonch.2016.07.001.
[8] H. Wang, Y. Shen, C. Shen, Y. Wen, H. Li, Enhanced adsorption of dye on magnetic Fe_3O_4 via HCl-assisted sonication pretreatment, Desalination 284 (2012) 122–127, https://doi.org/10.1016/j.desal.2011.08.045.
[9] M. Jafari, M.R. Rahimi, M. Ghaedi, H. Javadian, A. Asfaram, Fixed-bed column performances of azure-II and auramine-O adsorption by Pinus eldarica stalks activated carbon and its composite with zno nanoparticles: optimization by response surface methodology based on central composite design, J. Colloid Interface Sci. 507 (2017) 172–189, https://doi.org/10.1016/j.jcis.2017.07.056.
[10] D.D. Milenković, P.V. Dašić, V.B. Veljković, Ultrasound-assisted adsorption of copper(II) ions on hazelnut shell activated carbon, Ultrason. Sonochem. 16 (2009) 557–563, https://doi.org/10.1016/j.ultsonch.2008.12.002.
[11] M. Ghaedi, S. Hajjati, Z. Mahmudi, I. Tyagi, S. Agarwal, A. Maity, V.K. Gupta, Modeling of competitive ultrasonic assisted removal of the dyes - Methylene blue and Safranin-O using Fe_3O_4 nanoparticles, Chem. Eng. J. 268 (2015) 28–37, https://doi.org/10.1016/j.cej.2014.12.090.
[12] M. Ghaedi, F. Karimi, B. Barazesh, R. Sahraei, A. Daneshfar, Removal of reactive orange 12 from aqueous solutions by adsorption on tin sulfide nanoparticle loaded on activated carbon, J. Ind. Eng. Chem. 19 (2013) 756–763, https://doi.org/10.1016/j.jiec.2012.10.010.
[13] F.N. Azad, M. Ghaedi, K. Dashtian, S. Hajati, V. Pezeshkpour, Ultrasonically assisted hydrothermal synthesis of activated carbon-HKUST-1-MOF hybrid for efficient simultaneous ultrasound-assisted removal of ternary organic dyes and antibacterial investigation: Taguchi optimization, Ultrason. Sonochem. 31 (2016) 383–393, https://doi.org/10.1016/j.ultsonch.2016.01.024.
[14] M. Roosta, M. Ghaedi, A. Daneshfar, R. Sahraei, A. Asghari, Optimization of the ultrasonic assisted removal of methylene blue by gold nanoparticles loaded on activated carbon using experimental design methodology, Ultrason. Sonochem. 21 (2014) 242–252, https://doi.org/10.1016/j.ultsonch.2013.05.014.
[15] A. Durán, J.M. Monteagudo, I. Sanmartín, A. García-Díaz, Sonophotocatalytic mineralization of antipyrine in aqueous solution, Appl. Catal. B Environ. 138–139 (2013) 318–325, https://doi.org/10.1016/j.apcatb.2013.03.013.
[16] H. Askari, M. Ghaedi, K. Dashtian, M.H.A. Azghandi, Rapid and high-capacity ultrasonic assisted adsorption of ternary toxic anionic dyes onto MOF-5-activated carbon: artificial neural networks, partial least squares, desirability function and isotherm and kinetic study, Ultrason. Sonochem. 37 (2017) 71–82, https://doi.org/10.1016/j.ultsonch.2016.10.029.

[17] A. Asfaram, M. Ghaedi, H. Javadian, A. Goudarzi, Cu- and S- @SnO_2 nanoparticles loaded on activated carbon for efficient ultrasound assisted dispersive μSPE-spectrophotometric detection of quercetin in Nasturtium officinale extract and fruit juice samples: CCD-RSM design, Ultrason. Sonochem. 47 (2018) 1–9, https://doi.org/10.1016/j.ultsonch.2018.04.008.

[18] A. Elliott, T. Mahmood, Pretreatment technologies for advancing anaerobic digestion of pulp and paper biotreatment residues, Water Res. 41 (2007) 4273–4286, https://doi.org/10.1016/j.watres.2007.06.017.

[19] W.P. Barber, The effects of ultrasound on sludge digestion, Water Environ. J. 19 (2005) 2–7.

[20] B. Yin, S. Zhang, Y. Jiao, Y. Liu, F. Qu, X. Wu, Facile synthesis of ultra long MnO_2 nanowires as high performance supercapacitor electrodes and photocatalysts with enhanced photocatalytic activities, CrystEngComm 16 (2014) 9999–10005, https://doi.org/10.1039/C4CE01302F.

[21] J. Tang, B. Mu, W. Wang, M. Zheng, A. Wang, Fabrication of manganese dioxide/carbon/attapulgite composites derived from spent bleaching earth for adsorption of Pb(II) and Brilliant green, RSC Adv. 6 (2016) 36534–36543, https://doi.org/10.1039/c5ra26362j.

[22] N. Caliskan, A.R. Kul, S. Alkan, E.G. Sogut, I. Alacabey, Adsorption of Zinc(II) on diatomite and manganese-oxide-modified diatomite: a kinetic and equilibrium study, J. Hazard. Mater. 193 (2011) 27–36, https://doi.org/10.1016/j.jhazmat.2011.06.058.

[23] J. Mei, L. Zhang, Y. Niu, Fabrication of the magnetic manganese dioxide/graphene nanocomposite and its application in dye removal from the aqueous solution at room temperature, Mater. Res. Bull. 70 (2015) 82–86, https://doi.org/10.1016/j.materresbull.2015.04.021.

[24] Y. Xin, X. Long, M. Huang, X. Dong, Y. Yuan, C. Hua, Engineering birnessite-type MnO_2 nanosheets on fi berglass for pH-dependent degradation of methylene blue, J. Phys. Chem. Solids 83 (2015) 40–46, https://doi.org/10.1016/j.jpcs.2015.03.015.

[25] A. Asfaram, M. Ghaedi, S. Agarwal, I. Tyagi, V.K. Gupta, Removal of basic dye Auramine-O by ZnS: Cu nanoparticles loaded on activated carbon: optimization of parameters using response surface methodology with central composite design, RSC Adv. 5 (2015) 18438–18450, https://doi.org/10.1039/c4ra15637d.

[26] W. Au, S. Pathak, C.J. Collie, T.C. Hsu, Cytogenetic toxicity of gentian violet and crystal violet on mammalian cells in vitro, Mutat. Res. Toxicol. 58 (1978) 269–276, https://doi.org/10.1016/0165-1218(78)90019-8.

[27] W. Azmi, R.K. Sani, U.C. Banerjee, Biodegradation of triphenylmethane dyes, Enzyme Microb. Technol. 22 (1998) 185–191, https://doi.org/10.1016/S0141-0229(97)00159-2.

[28] B.P. Cho, T. Yang, L.R. Blankenship, J.D. Moody, M. Churchwell, F.A. Beland, S.J. Culp, Synthesis and characterization of N -demethylated metabolites of malachite green and leucomalachite green, Chem. Res. Toxicol. 285–294 (2003).

[29] M. Arash Asfaram, G.R. Ghaedi, F. Pepe Ghezelbashb, Application of experimental design and derivative spectrophotometry methods in optimization and analysis of biosorption of binary mixtures of basic dyes from aqueous solutions, Ecotoxicol. Environ. Saf. 139 (2017) 219–227.

[30] R. Ahmad, Studies on adsorption of crystal violet dye from aqueous solution onto coniferous pinus bark powder (CPBP), J. Hazard. Mater. 171 (2009) 767–773, https://doi.org/10.1016/j.jhazmat.2009.06.060.

[31] R. Azargohar, A.K. Dalai, Production of activated carbon from Luscar char: experimental and modeling studies, Microporous Mesoporous Mater. 85 (2005) 219–225, https://doi.org/10.1016/j.micromeso.2005.06.018.

[32] A. Asfaram, M. Ghaedi, S. Hajati, A. Goudarzi, Ternary dye adsorption onto MnO_2 nanoparticle-loaded activated carbon: derivative spectrophotometry and modeling, RSC Adv. 5 (2015) 72300–72320, https://doi.org/10.1039/C5RA10815B.

[33] Y. Wang, X.X. Zhang, X. He, W. Zhang, X.X. Zhang, C. Lu, In situ synthesis of MnO_2 coated cellulose nanofibers hybrid for effective removal of methylene blue, Carbohydr. Polym. 110 (2014) 302–308, https://doi.org/10.1016/j.carbpol.2014.04.008.

[34] A. Palinska, A. Grodzka, H. Elzanowska, B. Kepska, E. Zwierkowska, S. Achmatowicz, M. Maj-Zurawska, Methylene blue interactions with chromosomal and plasmid dna on screen-printed carbon electrodes, Electroanalysis 22 (2010) 1306–1313, https://doi.org/10.1002/elan.200900278.

[35] J. Mei, L. Zhang, Ultrasonic-assisted self-assembly synthesis of highly dispersed β-MnO_2 nano-branches interwoven with graphene flakes for catalytic oxidation of aromatic compounds, RSC Adv. 5 (2015) 14843–14850, https://doi.org/10.1039/C4RA16676K.

[36] W. Zhang, W. Zhao, Z. Zhou, Z. Yang, Facile synthesis of α-MnO_2 micronests composed of nanowires and their enhanced adsorption to Congo red, Front. Chem. Sci. Eng. 8 (2014) 64–72, https://doi.org/10.1007/s11705-014-1402-5.

[37] A. Reza, M. Ghaedi, A. Asfaram, R. Jannesar, A. Goudarzi, Design and construction of nanoscale material for ultrasonic assisted adsorption of dyes: application of derivative spectrophotometry and experimental design methodology, Ultrason. Sonochem. 35 (2017) 112–123.

[38] S. Porhemmat, M. Ghaedi, A. Reza, Nanocomposites: synthesis, characterization and its application to removal azo dyes using ultrasonic assisted method: modeling and optimization, Ultrason. Sonochem. 38 (2017) 530–543.

[39] S. Dashamiri, M. Ghaedi, A. Asfaram, F. Zare, S. Wang, Multi-response optimization of ultrasound assisted competitive adsorption of dyes onto Cu (OH) 2 -nanoparticle loaded activated carbon: central composite design, Ultrason. Sonochem. 34 (2017) 343–353.

[40] M. Saad, H. Tahir, J. Khan, U. Hameed, A. Saud, Synthesis of polyaniline nanoparticles and their application for the removal of Crystal Violet dye by ultrasonicated adsorption process based on Response Surface Methodology, Ultrason. Sonochem. 34 (2017) 600–608.

[41] E. Sharifpour, H. Haddadi, M. Ghaedi, Optimization of simultaneous ultrasound assisted toxic dyes adsorption conditions from single and multi-components using central composite design: application of derivative spectrophotometry and evaluation of the kinetics and isotherms, Ultrason. Sonochem. 36 (2017) 236–245, https://doi.org/10.1016/j.ultsonch.2016.11.011.

[42] K. Yu, Y. Liu, D. Lei, Y. Jiang, Y. Wang, Y. Feng, L. Lou, S. Liu, M3 + O (-Mn 4+)2 Clusters in Doped MnOx Catalysts as Promoted Active Sites for Aerobic Oxidation of 5-Hydroxymethylfurfural (2018) 1–10.

[43] K.B. Sutradhar, S. Khatun, I.P. Luna, Increasing possibilities of nanosuspension, J. Nanotechnol. 2013 (2013), https://doi.org/10.1155/2013/346581.

[44] B. Belhamdi, Z. Merzougui, M. Trari, A. Addoun, A kinetic, equilibrium and thermodynamic study of L-phenylalanine adsorption using activated carbon based on agricultural waste (date stones), J. Appl. Res. Technol. 14 (2016) 354–366, https://doi.org/10.1016/j.jart.2016.08.004.

[45] E.M. Fakhry, Padina pavonica for the removal of dye from polluted water, Am. J. Plant Sci. 4 (2013) 1983–1989.

[46] C. Muthukumaran, V. Murugaiyan, Adsorption isotherms and kinetic studies of crystal violet dye removal from aqueous solution using surfactant modified magnetic nanoadsorbent, J. Taiwan Inst. Chem. Eng. 63 (2016) 354–362, https://doi.org/10.1016/j.jtice.2016.03.034.

[47] A. Mittal, J. Mittal, A. Malviya, D. Kaur, V.K. Gupta, Adsorption of hazardous dye crystal violet from wastewater by waste materials, J. Colloid Interface Sci. 343 (2010) 463–473, https://doi.org/10.1016/j.jcis.2009.11.060.

[48] M.E. Mahmoud, G.M. Nabil, N.M. El-Mallah, H.I. Bassiouny, S. Kumar, T.M. Abdel-Fattah, Kinetics, isotherm, and thermodynamic studies of the adsorption of reactive red 195 A dye from water by modified Switchgrass Biochar adsorbent, J. Ind. Eng. Chem. 37 (2016) 156–167, https://doi.org/10.1016/j.jiec.2016.03.020.

[49] S. Shoukat, H.N. Bhatti, M. Iqbal, S. Noreen, Mango stone biocomposite preparation and application for crystal violet adsorption: a mechanistic study, Microporous Mesoporous Mater. 239 (2017) 180–189, https://doi.org/10.1016/j.micromeso.2016.10.004.

[50] T.M. Elmorsi, Equilibrium isotherms and kinetic studies of removal of methylene blue dye by adsorption onto miswak leaves as a natural adsorbent, J. Environ. Prot. (Irvine, Calif) 2 (2011) 817–827, https://doi.org/10.4236/jep.2011.26093.

[51] V. Saruchi, Kumar, Adsorption kinetics and isotherms for the removal of rhodamine B dye and Pb+2 ions from aqueous solutions by a hybrid ion-exchanger, Arab. J. Chem. (2016), https://doi.org/10.1016/j.arabjc.2016.11.009.

[52] M. Zhou, X. Zhang, L. Wang, J. Wei, L. Wang, K. Zhu, B. Feng, Growth process and microwave absorption properties of nanostructured γ-MnO_2 urchins, Mater. Chem. Phys. 130 (2011) 1191–1194, https://doi.org/10.1016/j.matchemphys.2011.08.056.

[53] A. Xie, F. Tao, C. Jiang, W. Sun, Y. Li, L. Hu, X. Du, S. Luo, C. Yao, A coralliform-structured γ -MnO_2/polyaniline nanocomposite for high-performance supercapacitors, J. Electroanal. Chem. 789 (2017) 29–37.

[54] C.D.A. Dias, H. De Santana, The relation between structural features and electrochemical activity of MnO_2 nanoparticles synthesized from a polyol-made Mn_3O_4 precursor, J. Solid State Electrochem. 17 (2013) 1967–1976, https://doi.org/10.1007/s10008-013-2043-1.

[55] R. Yang, Z. Wang, L. Dai, L. Chen, Synthesis and characterization of single-crystalline nanorods of α-MnO_2 and γ-MnOOH, Mater. Chem. Phys. 93 (2005) 149–153, https://doi.org/10.1016/j.matchemphys.2005.03.006.

[56] X. Ge, J. Liu, X. Song, G. Wang, H. Zhang, Y. Zhang, H. Zhao, Hierarchical iron containing γ-MnO_2 hollow microspheres: a facile one-step synthesis and effective removal of As(III) via oxidation and adsorption, Chem. Eng. J. 301 (2016) 139–148, https://doi.org/10.1016/j.cej.2016.05.005.

[57] S. Devaraj, N. Munichandraiah, Effect of crystallographic structure of MnO_2 on its electrochemical capacitance properties, J. Phys. Chem. C 112 (2008) 4406–4417.

[58] P. De Wolff, Interpretation of Some gamma -MnO_2 diffraction patterns, Acta Cryst. 12 (1959) 341–345.

[59] P.V. Shinde, Q.X. Xia, B.G. Ghule, N.M. Shinde, J. Seonghee, K.H. Kim, R.S. Mane, Hydrothermally grown α-MnO_2 interlocked mesoporous micro-cubes of several nanocrystals as selective and sensitive nitrogen dioxide chemoresistive gas sensors, Appl. Surf. Sci. 442 (2018) 178–184, https://doi.org/10.1016/j.apsusc.2018.02.144.

[60] D.N. Thanh, M. Singh, P. Ulbrich, F. Štěpánek, N. Strnadová, As(V) removal from aqueous media using α-MnO_2 nanorods-impregnated laterite composite adsorbents, Mater. Res. Bull. 47 (2012) 42–50, https://doi.org/10.1016/j.materresbull.2011.10.004.

[61] L. Feng, Z. Xuan, H. Zhao, Y. Bai, J. Guo, C. Su, X. Chen, MnO_2 prepared by hydrothermal method and electrochemical performance as anode for lithium-ion battery, Nanoscale Res. Lett. 1–8 (2014).

[62] H. Chen, Y. Wang, Y.-K. Lv, Catalytic oxidation of NO over MnO_2 with different crystal structures, RSC Adv. 6 (2016) 54032–54040, https://doi.org/10.1039/C6RA10103H.

[63] C.M. Julien, M. Massot, Vibrational spectroscopy of electrode materials for rechargeable lithium batteries IV. Lithium Metal Phosphates in: Proc. Int. Work. “Advanced Tech. Energy Sources Investig. Testing” 4 – 9 Sept., 2004 Sofia, Bulg. (2004).

[64] Kaori Matsuo, Katsuyuki Nakano, Characterization of semiconductor oxides by IR diffuse reflectance spectroscopy, Appl. Surf. Sci. 41 (42) (1990) 53–56.

[65] T. Wang, S. Chen, H. Wang, Z. Liu, Z. Wu, In-plasma catalytic degradation of toluene over different MnO_2 polymorphs and study of reaction mechanism, Cuihua Xuebao/Chinese, J. Catal. 38 (2017) 793–804, https://doi.org/10.1016/S1872-2067(17)62808-0.

[66] J. Zhang, Y. Li, L. Wang, C. Zhang, H. He, Catalytic oxidation of formaldehyde over manganese oxides with different crystal structures, Catal. Sci. Technol. 5 (2015) 2305–2313, https://doi.org/10.1039/C4CY01461H.

[67] M.C. Biesinger, B.P. Payne, A.P. Grosvenor, L.W.M. Lau, A.R. Gerson, R.S.C. Smart, Resolving surface chemical states in XPS analysis of first row transition metals, oxides and hydroxides: Cr, Mn, Fe, Co and Ni, Appl. Surf. Sci. 257 (2011) 2717–2730, https://doi.org/10.1016/j.apsusc.2010.10.051.
[68] V.P. Santos, M.F.R. Pereira, J.J.M. Órfão, J.L. Figueiredo, The role of lattice oxygen on the activity of manganese oxides towards the oxidation of volatile organic compounds, Appl. Catal. B Environ. 99 (2010) 353–363, https://doi.org/10.1016/j.apcatb.2010.07.007.
[69] M. Toupin, T. Brousse, D. Bélanger, Charge storage mechanism of MnO_2 electrode used in aqueous electrochemical capacitor, Chem. Mater. 16 (2004) 3184–3190, https://doi.org/10.1021/cm049649j.
[70] M. Chigane, M. Ishikawa, M. Izaki, Preparation of manganese oxide thin films by electrolysis/chemical deposition and electrochromism, J. Electrochem. Soc. 148 (2001) D96, https://doi.org/10.1149/1.1376637.
[71] D.B. Munuswamy, V.R. Madhavan, M. Mohan, Synthesis and surface area determination of alumina nanoparticles by chemical combustion method, Int. J. ChemTech Res. 8 (2015) 413–419.
[72] A.M. Ealias, M.P. Saravanakumar, Facile synthesis and characterisation of AlNs using Protein Rich Solution extracted from sewage sludge and its application for ultrasonic assisted dye adsorption: isotherms, kinetics, mechanism and RSM design, J. Environ. Manage. 206 (2018) 215–227.
[73] V. Mathew, J. Lim, J. Kang, J. Gim, A.K. Rai, J. Kim, Electrochemistry communications self-assembled mesoporous manganese oxide with high surface area by ambient temperature synthesis and its enhanced electrochemical properties, Electrochem. Commun. 13 (2011) 730–733, https://doi.org/10.1016/j.elecom.2011.04.023.
[74] H.L. Parker, A.J. Hunt, V.L. Budarin, P.S. Shuttleworth, K.L. Miller, J.H. Clark, The importance of being porous: polysaccharide-derived mesoporous materials for use in dye adsorption, RSC Adv. 2 (2012) 8992–8997, https://doi.org/10.1039/c2ra21367b.
[75] J. de S. Macedo, N.B. da Costa Júnior, L.E. Almeida, E.F.da S. Vieira, A.R. Cestari, I. de F. Gimenez, N.L. Villarreal Carreño, L.S. Barreto, Kinetic and calorimetric study of the adsorption of dyes on mesoporous activated carbon prepared from coconut coir dust, J. Colloid Interface Sci. 298 (2006) 515–522, https://doi.org/10.1016/j.jcis.2006.01.021.
[76] M. Iwasaki, M. Kita, K. Ito, A. Kohno, K. Fukunishi, Intercalation characteristics of 1,1'-diethyl-2,2'-cyanine and other cationic dyes in synthetic saponite: Orientation in the interlayer, Clays Clay Miner. 48 (2000) 392–399, https://doi.org/10.1346/CCMN.2000.0480310.
[77] P. Pal, S.K. Pahari, A.K. Giri, S. Pal, H.C. Bajaj, A.B. Panda, Hierarchically order porous lotus shaped nano-structured MnO_2 through $MnCO_3$: chelate mediated growth and shape dependent improved catalytic activity, J. Mater. Chem. A 1 (2013) 10251, https://doi.org/10.1039/c3ta11440f.
[78] A.L. Bojic, V.B. Veljkovic, Ultrasound-assisted adsorption of 4-dodecylbenzene sulfonate from aqueous solutions by corn cob activated carbon, Ultrason. Sonochem. 20 (2013) 955–962.
[79] D. Zhao, M. Li, D. Zhang, S. Ali, X. Xu, Reductive dechlorination of 2, 4-dichlorophenol by Pd/Fe nanoparticles prepared in the presence of ultrasonic irradiation, Ultrason. Sonochem. 20 (2013) 864–871.
[80] Y.S. Ho, G. McKay, Pseudo-second order model for sorption processes, Process Biochem. 34 (1999) 451–465, https://doi.org/10.1016/S0032-9592(98)00112-5.
[81] X. Luo, S. Zhang, X. Lin, New insights on degradation of methylene blue using thermocatalytic reactions catalyzed by low-temperature excitation, J. Hazard. Mater. 260 (2013) 112–121, https://doi.org/10.1016/j.jhazmat.2013.05.005.
[82] J. Cheriaa, M. Khaireddine, M. Rouabhia, A. Bakhrouf, Removal of triphenylmethane dyes by bacterial consortium, Sci. World J. 2012 (2012) 1–9, https://doi.org/10.1100/2012/512454.
[83] H.J. Kumari, P. Krishnamoorthy, T.K. Arumugam, S. Radhakrishnan, D. Vasudevan, An efficient removal of crystal violet dye from waste water by adsorption onto TLAC/Chitosan composite: a novel low cost adsorbent, Int. J. Biol. Macromol. 96 (2017) 324–333, https://doi.org/10.1016/j.ijbiomac.2016.11.077.Sulphuric.
[84] W.H. Kuan, C.Y. Chen, C.Y. Hu, Removal of methylene blue from water by γ-MnO_2, Water Sci. Technol. 64 (2011) 899–903, https://doi.org/10.2166/wst.2011.262.
[85] W.H. Kuan, Y.C. Chan, PH-dependent mechanisms of methylene blue reacting with tunneled manganese oxide pyrolusite, J. Hazard. Mater. 239–240 (2012) 152–159, https://doi.org/10.1016/j.jhazmat.2012.08.051.
[86] L. Zhang, H. Zhang, W. Guo, Y. Tian, Removal of malachite green and crystal violet cationic dyes from aqueous solution using activated sintering process red mud, Appl. Clay Sci. 93–94 (2014) 85–93, https://doi.org/10.1016/j.clay.2014.03.004.
[87] V.A. Online, L. Chen, J. Ding, Adsorption behavior of magnetic amino-functionalized metal-organic framework for cationic and anionic dyes from aqueous solution, RSC Adv. (2016), https://doi.org/10.1039/C6RA07567C.
[88] S. Ferdous, M.A. Ioannidis, D. Henneke, Effects of temperature, pH, and ionic strength on the adsorption of nanoparticles at liquid – liquid interfaces, J. Nanopart. Res. (2012), https://doi.org/10.1007/s11051-012-0850-4.
[89] Y. Zhao, J. Geng, X. Wang, X. Gu, S. Gao, Adsorption of tetracycline onto goethite in the presence of metal cations and humic substances, J. Colloid Interface Sci. 361 (2011) 247–251, https://doi.org/10.1016/j.jcis.2011.05.051.
[90] H. Liu, Y. Dong, H. Wang, Y. Liu, Ammonium adsorption from aqueous solutions by strawberry leaf powder: equilibrium, kinetics and effects of coexisting ions, Desalination 263 (2010) 70–75, https://doi.org/10.1016/j.desal.2010.06.040.
[91] S. Wang, T. Terdkiatburana, M.O. Tadé, Adsorption of Cu(II), Pb(II) and humic acid on natural zeolite tuff in single and binary systems, Sep. Purif. Technol. 62 (2008) 64–70, https://doi.org/10.1016/j.seppur.2008.01.004.
[92] M. Wang, Ultrasound Induced Microalgal Cell Disruption: Experimental and Computational Research, 2015.
[93] W. Zhang, M. Deng, C. Sun, S. Wang, Ultrasound-enhanced adsorption of chromium (VI) on Fe_3O_4 magnetic particles, Ind. Eng. Chem. Res. 53 (2014) 333–339.
[94] M. Breitbach, D. Bathen, Effect of ultrasound on adsorption and desorption processes, Ind. Eng. Chem. 42 (2003) 5635–5646.
[95] R.L. Tseng, P.H. Wu, F.C. Wu, R.S. Juang, Half-life and half-capacity concentration approach for the adsorption of 2,4-dichlorophenol and methyl blue from water on activated carbons, J. Taiwan Inst. Chem. Eng. 42 (2011) 312–319, https://doi.org/10.1016/j.jtice.2010.07.002.
[96] F. Wu, R. Tseng, S. Huang, R. Juang, Characteristics of pseudo-second-order kinetic model for liquid-phase adsorption: a mini-review, Chem. Eng. J. 151 (2009) 1–9, https://doi.org/10.1016/j.cej.2009.02.024.
[97] H. Qiao, Y. Zhou, F. Yu, E. Wang, Y. Min, Q. Huang, L. Pang, T. Ma, Effective removal of cationic dyes using carboxylate-functionalized cellulose nanocrystals, Chemosphere 141 (2015) 297–303.
[98] J. Zhang, F. Li, Q. Sun, Rapid and selective adsorption of cationic dyes by a unique metal-organic framework with decorated pore surface, Appl. Surf. Sci. 440 (2018) 1219–1226.
[99] M. Sathya, P.E. Kumar, M. Santhi, E. Arts, E. Arts, Isotherm studies for the adsorption of a acid green, Int. J. Sci. Environ. Technol. 6 (2017) 2955–2965.
[100] M. Santhi, P.E. Kumar, B. Muralidharan, Removal of malachite green dyes by adsorption onto activated carbon – Mno 2 – nanocomposite – kinetic study and equilibrium isotherm analyses, IOSR J. Appl. Chem. 8 (2015) 33–41, https://doi.org/10.9790/5736-08413341.